UNIVERSIDADE DE LISBOA
FACULDADE DE CIÊNCIAS
DEPARTAMENTO DE FÍSICA

Perfusion MRI quantification for Multi-Echo EPIK sequence in brain tumour patients

Filipa Soares da Silva

Mestrado Integrado em Engenharia Biomédica e Biofísica
Perfil em Engenharia Clínica e Instrumentação Médica

Dissertação orientada por:
Prof. Doutor Nuno Matela
Doutor Seong Dae Yun

2018

Acknowledgements

First of all, my gratitude goes to Professor Jon Shah for giving me the opportunity to work at the Institute of Neurosciences and Medicine of the Forschungszentrum Jülich in INM-4. It was a privilege to work there. I am thankful to be part of such important research group and to experience a real research environment. The funding received from the student program for the last six months of the internship was essential for this project.

In addition, I would like to thank Doctor Yun Seong Dae for giving me the opportunity to work with him in this project. I am grateful for all he taught me, for all the given advice, time and patience spent on my work.

I would also like to express my gratitude to Liliana Caldeira who welcomed me in the Institute and not only guided me through my stay, but also eased my arrival.

Furthermore, Professor Nuno Matela also has my gratitude, since it was him who first introduced me to this fascinating topic and prestigious institute. Although not a constant presence due to the existent distance, he was always reachable and prompt to help, support and provide feedback whenever required. He was someone who helped me path my future and I hope I can always count on his guidance.

I would like to thank the staff of the Institute of Neurosciences and Medicine of the Forschungszentrum Jülich for providing me with the conditions to learn more about neurosciences and for all their sympathy and encouragement during my stay. A special thanks to INM-4 and MR/PET physics group for all your support and interesting discussions.

I would like to express my deepest gratitude to the Professors of the Institute of Biophysics and Biomedical Engineering for all the time, sympathy, encouragement and knowledge during the last five years. Once again, the funding I received from the Erasmus Program was essential for this project.

This work was only possible with the support of my family. A special thanks to my parents, grandparents, uncles and aunt for their moral support and encouragement, not only during this work but also throughout my academic path. Without their help, I would not have been able to neither start nor finish

this journey.

Finally, a warm thank you from the bottom of my heart to both my old and new friends. I am grateful to those who encouraged me while I left to another country and welcomed me again as I returned. I am grateful to those I met in this journey, as they made my stay abroad much more exciting and blissful. A kind word to my flatmate and friend. It was a year really full of colour.

Abstract

The main goal of this thesis was to obtain fully quantifying perfusion parameters from both DSC (Dynamic Susceptibility Contrast) and DCE (Dynamic Contrast Enhancement) techniques through usage of only one perfusion sequence – GESE EPIK (Gradient-echo, Spin-echo Echo-Planar Imaging with Keyhole). For this, twenty-two patients with a possible brain tumor were recruited for this study, and each patient was scanned at a hybrid PET-MR 3T scanner. Firstly, T_1-mapping data was acquired through a sequence of Inversion-Recovery EPIK. The contrast agent was then injected into the patient and perfusion images were acquired using the GESE EPIK sequence. Simultaneously, ^{18}F-FET images were acquired which allowed the exclusion of patients who did not have any brain tumor.

After the images were acquired, they were analyzed and the parameters were calculated. For starters, the information regarding the changes in T_2 and $T_2{}^*$, already inherent to the data acquired, was analyzed. The curve of the MR signal was converted to the concentration curve. This curve was calculated using two different equations. With the calculated concentration curve, the DSC parameters were calculated. As expected, in areas affected by a tumor, there was an increase in vascularization due to angiogenesis. It was also observed, by comparison of the two methods used to calculate the concentration curves, that the non-removal of the leakage effects induced an unreal increase in the calculated parameters.

In order to obtain images related to variations of T_1 for DCE quantification, the images acquired were extrapolated to a echo time equal to zero. To these extrapolated images, the values obtained from the T_1-mapping prior to the contrast's injection were subtracted in order to obtain the concentration curve. A method that used the extrapolated images to obtain an initial T_1-mapping was also tested, in order to avoid the need to implement the extra sequence for that purpose. The Tofts kinetic model was applied in both methods, allowing the calculation of DCE parameters. In both applied methods, the results obtained were very similar, indicating the possibility of non-acquisition of the extra sequence if there are time constraints. However, not all parameters behaved as expected and a more detailed investigation of the literature was carried out. It is concluded that some parameters do not have a clear description and cannot characterize human physiology and be used in the study of pathologies.

In conclusion, the initial goal of this thesis to obtain quantitative parameters DSC and DCE perfusion techniques, using only a single contrast sequence, was achieved with success. The need to remove leakage effects, which increased the calculated values and the tumor area, was also verified. However, some inconsistencies in the parameters' interpretation were registered in the available literature. These inconsistencies had repercussions in some values obtained, whose interpretation was impossible, despite being in agreement with the literature. In addition, a method has been tested which further eliminates the need to acquire T_1-mapping data prior to the contrast's injection through an additional sequence. Although not an objective of this thesis, it was not possible to relate the perfusion parameters to the degree of tumor severity.

Key-words: MR-PET; Perfusion MRI; GESE-EPIK; DSC; DCE.

Resumo

Ressonância magnética de perfusão é um termo utilizado para se referir a uma variedade de técnicas de ressonância que permitem obter informação relativa ao grau de vascularização dos tecidos examinados. É baseada no princípio de Fick que define que o fluxo de sangue a um órgão pode ser calculado se for do nosso conhecimento a quantidade de agente marcador que o órgão examinado absorve, recebe e expele. Este agente marcador pode ser inerente ao próprio corpo ou ser injetado. Se for injetado é tipicamente referido como agente de contraste e trata-se de um componente químico à base de Gadolínio. As técnicas que necessitam de injeção deste contraste são DCE e DSC.

DSC, um acrónimo inglês de Dynamic Contrast Susceptibility, utiliza métodos de rápida aquisição de imagens para delinear o movimento do agente de contraste na circulação sanguínea do órgão de interesse, após injeção. É uma técnica dependente da magnetização transversal, T_2 ou T_2^*, e, após aquisição das imagens, um modelo cinético é aplicado de forma a se obter parâmetros caracterizantes da perfusão dos tecidos. Desses parâmetros, no caso do volume de interesse ser o cérebro, destaca-se o volume sanguíneo cerebral (CBV, acrónimo inglês de Cerebral Blood Volume), o fluxo sanguíneo cerebral (CBF, acrónimo inglês de Cerebral Blood Flow) e o rácio entre eles (MTT, acrónimo inglês de Mean Transit Time). Estes parâmetros estão intimamente relacionados com a presença de tumores, sendo identificativos dessa patologia dado que zonas afetadas por gliomas tendem a registar um aumento anormal da vascularização por presença dessa mesma patologia.

Semelhantemente, DCE, acrónimo inglês de Dynamic contrast enhancment, avalia a absorção de contraste pelo tecido, através da evolução da magnetização longitudinal, T_1. Nesta técnica, para além da aquisição de dados após injeção do contraste, é necessário adquirir uma imagem anatómica informativa dos valores da magnetização longitudinal prévia à injeção da substância marcadora, denominado de T_1-mapping. Esta aquisição extra permite o cálculo de parâmetros quantificativos de perfusão do tecido, que, de outra forma, seriam apenas relativos. Os parâmetros calculados dependem ainda do modelo cinético aplicado aos dados adquiridos.

Dado que ambas as técnicas de ressonância magnética de perfusão fornecem informações complementares, foi do interesse de medicina adotar o uso de uma sequência de ressonância magnética que adquirisse informação tanto da magnetização longitudinal como da transversal. Uma sequência que permitisse tal aquisição foi desenvolvida no Forschungzentrum Jülich. Esta sequência denominada GESE explora as vantagens de aquisição da técnica de imagem Echo-planar Imaging with Keylohe (EPIK). Esta sequência permite obter imagens relativas às alterações da magnetização transversal, ao longo do tempo, e permite a extrapolação de imagens relativas às alterações da magnetização longitudinal devido ao número e tipo de ecos que a compõem. Desta forma, é possível obter imagens relativas a ambas as técnicas DSC e DCE. Esta dissertação tem como objetivo obter parametros quantitativos das duas técnicas de perfusão utilizando uma única sequência - GESE EPIK.

Para este estudo foram recrutados vinte e dois pacientes com possível presença de tumor cerebral, que, a pedido médico, necessitavam de um exame de ^{18}F-FET . Cada paciente foi injectado com uma dose de 0.1 mmol/kg de Gd-DTPA por peso corporal. As medições foram realizadas no scanner híbrido de MR-PET de 3T. O T_1-mapping foi adquirido em primeiro lugar através de uma sequência de Inversion-Recovery EPIK. Seguidamente, o agente de contraste foi injectado no paciente e as imagens de perfusão foram adquiridas usando a sequência GESE EPIK. Simultaneamente, foram adquiridas imagens de ^{18}F-FET que permitiram a exclusão de pacientes que afinal não apresentavam tumores cerebrais.

Após aquisição das imagens, estas foram analisadas e os parâmetros calculados. Iniciou-se pela análise da informação relativa a T_2 e T_2^*, já inerentes aos próprios dados adquiridos. A curva do sinal de RM foi convertida na curva de concentração. Esta curva foi calculada utilizando duas equações distintas de forma a permitir a verificação da influência da passagem do contraste para fora da corrente sanguínea no cálculo da curva. Foi calculada ainda a curva que representa a fornecimento do agente de contraste ao tecido estudado, por meios de um método automatizado desenvolvido no centro de investigação. Neste método, são procuradas as curvas com maior amplitude de sinal, ordenadas por ordem crescente de amplitude e com as últimas cinco (pode se optar por outro número) é calculada uma curva média. Esta curva é necessária para o cálculo dos parâmetros e é denominada por AIF (acrónimo inglês de Arterial Input Function). Com a curva de concentração calculada e a AIF, os parâmetros já referidos foram calculados. Como seria de se esperar, em zonas afetadas por um tumor, houve registo de um aumento da vascularização, devido à angiogénese. Observou-se ainda, por comparação dos dois métodos de cálculo das curvas de concentração, que a não remoção dos efeitos da passagem do contraste dos vasos para o tecido induz um acréscimo irreal nos parâmetros calculados.

De forma a obter imagens relativas às variações de T_1, as imagens obtidas foram extrapoladas para um tempo anterior à aquisição de forma a que projetassem informação da magnetização longitudinal. A estas imagens extrapoladas foram subtraídos os valores obtidos do T_1-mapping de forma a se obter uma curva de concentrações não relativas. Foi ainda testado um método que utilizava as imagens extrapoladas para

obter um T_1-mapping inicial de forma a evitar a necessidade da implementação da sequência extra para o efeito. Foi aplicado o modelo cinético de Tofts, explicativo da fisiologia inerente, em ambos os métodos utilizados, possibilitando o cálculo dos parâmetros K_{trans} e K_{ep}. Estes parâmetros são representativos do fluxo de substâncias entre os vasos sanguíneos e o plasma intercelular, ou seja, caracterizam a permeabilidade do tecido. Em ambos os métodos aplicados, os resultados obtidos foram muito semelhantes, indicando a possibilidade de não aquisição da sequência extra caso haja limitações do tempo de exame. No entanto, dos dois parâmetros obtidos, apenas o parâmetro K_{trans} se comportou como seria de esperar, tendo valores maiores em regiões tumorais. Já o parâmetro K_{ep} comportou-se de forma irregular, sendo que uma investigação mais aprofundada à literatura foi realizada e concluiu-se que este parâmetro não tem uma descrição consensual, não podendo assim ser caracterizante da fisiologia humana e utilizado com rigor no estudo de patologias.

Apesar de não ser um objetivo inicial, pensou-se em analisar os valores dos parâmetros e compará-los com a gravidade do tumor, de forma a perceber se havia alguma relação que permitisse a classificação do glioma sem necessidade de uma biopsia. No entanto, tal comparação não foi possível dado que não havia informação prévia do grau de severidade do tumor de cada paciente.

Em conclusão, o objetivo inicial desta tese de obter parâmetros quantitativos das duas técnicas de perfusão utilizando apenas uma única sequência de contraste foi atingido com algum sucesso. Comprovou-se ainda a necessidade de remoção dos efeitos de passagem do contraste da corrente sanguínea para os tecidos, que incrementavam os valores calculados e a área tumoral. No entanto, registou-se uma inconsistência na interpretação dos parâmetros em várias literaturas, provenientes da aplicação de modelos cinéticos cujos parâmetros foram introduzidos sem bases reais na fisiologia ou com incoerências na sua explicação. Estas inconsistências tiveram repercussões nalguns valores obtidos, cuja interpretação foi impossível, ainda que estivessem de acordo com a literatura. De realçar que a mesma literatura raramente interpretava os valores obtidos ou, quando o fazia, cada estudo tinha a sua interpretação, não havendo uma descrição fisiológica que justificasse os valores obtidos. Adicionalmente, testou-se um método que permite ainda excluir a aquisição de um T_1-mapping prévio à injeção do contraste, removendo a necessidade de uma sequência adicional e diminuindo o tempo de exame. Através da extrapolação do T_1-mapping, o tempo de exame diminui, o que pode ser essencial para certos pacientes. Ainda que não fosse um objetivo desta tese, não se conseguiu relacionar os parâmetros de perfusão com o grau de severidade tumoral. De forma a confirmar a realidade destes valores de perfusão sugeriu-se a criação de um phantoma de perfusão.

Palavras-Chave: MR-PET; Ressonância Magnética de Perfusão; GESE-EPIK; DSC; DCE.

Contents

List of Figures

List of Tables

List of Abbreviations

2D Two-dimensional

3D Three-dimensional

AIF Arterial Input Function

AUC Area Under the Curve

BBB Blood-Brain Barrier

CA Contrast Agent

CBF Cerebral Blood Flow

CBV Cerebral Blood Volume

CNS Central Nervous System

DCE Dynamic Contrast Enhancement

DSC Dynamic Susceptibility Contrast

CT Computed Tomography

FET Fluoro-Ethyl-Tyrosine

FID Free Induction Decay

FT Fourier Transform

EPI Echo-Planar Imaging

EPIK Echo-Planar Imaging with Keyhole

EES Extravascular-Extracelullar Space

GE Gradient-Echo

GESE Gradient-echo, Spin-echo

HGG High Grade Glioma

INM-4 Institute of Neuroscience and Medicine-4

IR Inversion Recovery

LGG Low Grade Glioma

LL Look-Locker

MR Magnetic Resonance

MRI Magnetic Resonance Imaging

MR-PET Magnetic Resonance-Positron Emission Tomography

MTT Mean Transit Time

NMR Nuclear Magnetic Resonance

PET Positron emission tomography

ROI Region of Interest

RF Radio-frequency

SAGE Spin and Gradient Echo

SE Spin-Echo

SNR Signal to Noise Ratio

SPECT Single-photon emission computed tomography

SVD Singular Value Decomposition

TE Echo-Time

TI Inversion-Time

TR Repetition-Time

WHO World Health Organization

Chapter 1

Context and Outline

1.1 Introduction

Imaging of brain hemodynamics and cerebral vascular parameters have been assessed by many imaging modalities such as computed tomography (CT) ([1], [2]), positron emission tomography (PET) ([3], [4]) and single photon emission computed tomography (SPECT) ([5]), among others. Every method has its advantages and disadvantages. For example, in CT there is high anatomic resolution, but limited immediate cortical enhancement following contrast injection which lessens its clinical usage. PET scans are superior to all other metabolic imaging methods in terms of resolution and imaging speed. However, some of the used radioisotopes have short half-lives and, therefore, decay rapidly, making it quite difficult to be used in a large number of institutions and limiting the exams' duration [6]. With the development of "ultra-fast" MR imaging techniques, a dynamic assessment of brain hemodynamics became possible in MRI, also known as perfusion MRI.

Perfusion MRI is a term used to refer to a variety of MRI techniques which assess the vascularization of the imaged tissue along with the delivery of oxygen and nutrients. In other words, perfusion MRI techniques trace the blood in order to give insight of the region vascularization. Arterial spin labeling is a perfusion technique in which contrast injection is not required. Meanwhile, for DSC and DCE an exogenous substance must be injected.

DCE and DSC techniques both require the injection of a contrast agent, typically Gadolinium based. While the contrast agent passes through the vasculature, it produces changes in the MR signal intensity that are then measured and used to study tissues' properties. Both techniques are used for brain tumor diagnosis and characterization. Several studies have even addressed the possibility of using derived perfusion parameters to grade the tumors ([7], [8], [9]).

Dynamic Susceptibility Contrast, DSC, is a technique usually based on a T_2- or T_2^*-weighted imaging sequence, with two-dimensional (2D) or three-dimensional (3D) dynamic acquisition [10]. The scan protocol can consist of a gradient-echo (GE) acquisition or a spin-echo (SE) acquisition. GE sequences

are more prone to static field inhomogeneities which result in signal losses. Meanwhile SE acquisitions compensate for the field inhomogeneities with a refocusing pulse.

Dynamic Contrast Enhancement, DCE, is a technique usually scanned with a T_1-weighted imaging sequence with 2D or 3D dynamic acquisition. GE measurements are sensitive to all vessel sizes, but SE measurements are more sensitive to small vessels. For quantitative DCE-MRI, a pre-contrast mapping of T_1 is often performed, or in clinical practice, in order to save scanning time, a constant baseline T_1 value is often used. For this, the most used sequences are inversion-recovery spin-echo sequence (IR-SE) or, alternatively, IR-SE with echo planar imaging (EPI) [11].

The parametric images extracted from both DSC and DCE are relevant to characterize tumors [7]. However, the clinical methodology used to acquire those parametric images is based on two independent pulse sequences – one for DSC and one for DCE ([8], [12]) – where each has its associated drawbacks. These sequences are single-shot GE EPI and spoiled GE, respectively. On one hand, single-shot GE EPI, for DSC, suffers from errors due to CA leakage, which often addressed with a pre-load injection prior to the actual measurement, increasing measurement time and amount of injected contrast agent [9]. This is an approach that reduces uncertainties but does not completely eliminate them [13]. On the other hand, T_1-weighted imaging using spoiled GE, used for DCE, requires a balanced trade-off between temporal resolution and brain coverage [8].

In order to overcome the need for two independent sequences and address some of the associated drawbacks, several techniques have been suggested to mitigate or eliminate all drawbacks. Among them were correction algorithms [14], a pre-dosage with a small amount of Gadolinium-based contrast agent [15], MRI pulse sequences that use excitation pulses with lower flip angles, or multi-echo GE perfusion MRI methods in which tracer concentrations are based on absolute $R_2{}^*(t)$ instead of its relative changes [16].

A method using a refocusing pulse after the first two echoes to obtain SE contrast has been proposed [17] and is called Spin and Gradient Echo (SAGE) or Gradient-echo, Spin-echo (GESE) DSC method. GESE DSC has been successfully demonstrated in humans to image different organs, and in small animals. However, this approach also has the usual limitations such as susceptibility artefacts and geometric distortions resulting from the single-shot EPI readout. Therefore, an alternative method for GESE DSC using EPIK was proposed in [18]. This method showed improvements in the perfusion measurements, having a reasonable trade-off between spatial/temporal resolution and brain coverage. By combining the first two echoes and extrapolation to TE=0, semi-quantitative T_1-based data related to DCE methods can be obtained.

This sequence, however, like the others before, only allows for semi-quantitative analyses of DCE-based parameters. To fully quantify the DCE-based parameters, a T_1 map prior to contrast injection is required, as already referred. This remains as one of the current challenges to completely overcome the need for two independent imaging sequences in brain perfusion imaging.

1.2 Thesis' Objectives and Outline

This master thesis project has two goals: i) to use the sequence SAGE EPIK with 5 echoes to acquire both DSC and DCE data and ii) to quantify both data-sets and obtain perfusion parameters specific to each

technique. To fully quantify DCE parameters, T_1-mapping previous to contrast injection is required. Therefore an additional sequence for this purpose was added and used. Although not a initial goal, a method for extrapolating the T_1-mapping was also tested in order to address the future possibility of only requiring the SAGE EPIK sequence.

This thesis is organized in seven chapters described below. The present Chapter 1 introduces the context, motivation and general organization of the work.

Chapter 2 introduces some relevant theoretic concepts for this work. MR physics, imaging principles and used hardware are firstly introduced, followed by MR sequences most relevant for this project. A small section in hybrid imaging was also included since all data was acquired in a PET-MR scanner and the PET images were used to filter patients without tumor from the data to be used for this project.

In Chapter 3, a brief introduction to brain tumors, particularly their severeness and grading are addressed.

Chapter 4 describes the two studied perfusion techniques - DCE and DSC - introducing the concepts and the methods used for the analyses of the acquired data. These analyses methods include both fully quantifying methods and non-quantifying methods for better understanding of the relevance of the first ones.

In Chapter 5, materials and methods developed in this dissertation are described. Patients' information, MRI and PET acquisitions along with MRI data analyses are addressed. This includes both perfusion techniques parameter derivation.

Chapter 6 presents the results obtained in this work from the methodologies explained in the previous chapter. The results are also interpreted and discussed in this chapter.

Finally, in Chapter 7, final conclusions are drawn and possible error sources are identified. Whether the goals were reached and what future work ought to be performed are also included in this final chapter.

Chapter 2

Magnetic Resonance Imaging

Magnetic resonance imaging (MRI) is a versatile imaging modality that is widely used in clinical practice for the diagnosis and evaluation of a broad range of disorders, including cancer [19][20]. MRI can non-invasively, and without the hazard of ionizing radiation, produce high resolution images in multiple (arbitrary) planes of the interior of the body. There are several types of MR images, some of which are exquisitely sensitive to subtle changes within soft tissues. Typically, MRI uses magnetic fields and radio frequency energy to acquire signals (that are then used to construct images) from hydrogen nuclei, contained mainly in tissue water. The contrast depicted in MR images is typically due to variations from tissue to tissue in the density of hydrogen nuclei, and/or in other MR properties such as the relaxation times T_1 and T_2, which largely depend on the macromolecular composition of tissues. In many pathologies, the intrinsic contrast between soft tissues is sufficiently great that often contrast agents are not needed or used with MRI. Nonetheless, to derive special contrasts for a particular MR application (e.g. angiography and perfusion), the use of exogenous contrast has been proven to be safe in many clinical imaging procedures [21].

2.1 Magnetic Resonance Physics

2.1.1 Nuclear Spin and Precession

The structure of an atom is an essential component of the MR experiment. For MRI, a particular type of nucleus is selected and its distribution throughout the body is evaluated. Hydrogen is the most commonly imaged element, not only due to its abundance in the body, but also because it gives the strongest MRI signal.

The hydrogen atom is a single proton which is not stationary, but actually spins around an axis as shown in Figure 2.1. This non-stationary property of these atoms is the source of the MRI signal. The spinning property of atomic and subatomic particles is known as **spin** or **spin angular momentum**. Although it is described as spin, the particle is not actually spinning or rotating. In fact, its rotational axis is constantly

changing, or in other words, its nucleus are **precessing**. The magnitude of spin is quantised, meaning that it can only take on a set of limited discrete values.

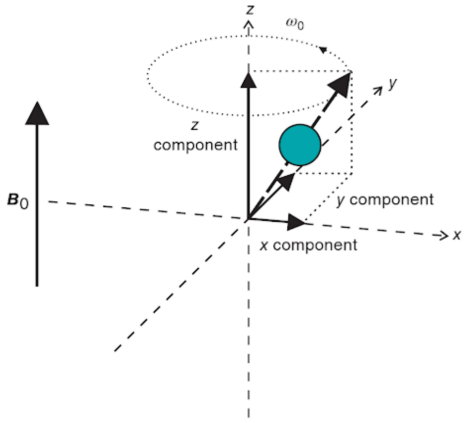

Figure 2.1: Classical representation of a proton precessing in a magnetic field of magnitude B_0. Adapted from [22].

Typically, in the human body, each of the hydrogen protons will have its spin axis orientated at random and their individual magnetic fields tend to cancel each other out. Their magnetic momentum, μ, and angular momentum, L, are related by:

$$\mu = \gamma L \tag{2.1}$$

, where γ is the gyro-magnetic ratio which is nuclei specific. In the presence of a static external magnetic field B_0, they preferably align themselves with the direction of the field. Their precession frequency will now be calculated by

$$w_L = \gamma B_0 \tag{2.2}$$

, the so called, Larmor frequency.

2.1.2 Bloch's Equations

The Bloch's equations are a set of equations that describe the behaviour of the macroscopic magnetization, M(t), in the presence of an external time-dependent magnetic field.
They were firstly introduced by Felix Bloch in 1964, whose name was given to the equation in honor of his discovery [23]. Bloch began with the assumption that the existent nuclei in a sample could be represented by a single vector, M(t), where this vector also possesses spin angular momentum. When this macroscopic sample is placed in a external magnetic field, the net magnetization will experience a torque force which can be described by Equation 2.3.

$$\frac{dM(t)}{d(t)} = \gamma[M(t) \times B(t)] \tag{2.3}$$

Further explanation of the Bloch equations and the origin of the MRI signal are devised in the two following subsections: excitation and relaxation.

2.1.2.1 Excitation

When an oscillating system, with its own frequency, is subjected to an external periodic stimulus and, if the forcing frequency equals its own natural frequency, the outcome will be its best possible - excitation. This is called the **resonance phenomenon**. This is the origin of the MRI signal; when a radio pulse with the Larmor frequency is applied, the protons resonate, absorb the energy and can then "flip" to high energy state. In addition, they are also forced to process in phase with the pulse.
When in an external magnetic field, the protons reach their magnetization within a few seconds and remain at that level unless they are disturbed by a change in the field or by pulses of radio-frequency (RF) energy. This radio frequency pulse is commonly referred to as an excitation pulse and typically contain a narrow range of or bandwidth of frequencies around a central frequency. During the pulse, the protons, as explained, absorb a portion of this energy at a particular frequency which is proportional to the B_0. Following the pulse, the protons re-emit the energy of the same frequency.
Considering M_0 the initial state of the representative vector M(t). The energy applied is an RF pulse with central frequency W_{RF} and orientation perpendicular to B_0, often addressed as B_1. The difference in orientation allows energy to be transferred to the protons. When $w_{RF} = w_L$, the RF energy is absorbed which causes M_0 to rotate away from its equilibrium orientation producing a transverse magnetic field.

2.1.2.2 Relaxation

After the applied RF, the excited protons will return to their original orientation in the B_0 field, by giving up the acquired extra energy, in a process known as relaxation.
While the system returns to the equilibrium state, an increase of longitudinal magnetization occurs, simultaneous to a decrease of the transverse magnetization.
The longitudinal magnetic field increases to its original state, recovering by energy transference from the protons to the surrounding macro-molecules. This energy exchange process is called **spin-lattice interaction**. This recovery is exponential and, when a 90° is applied, is characterized by a longitudinal relaxation time T_1 and Equation 2.4.

$$M_z(t) = M_z^0(1 - e^{-t/T_1}) \tag{2.4}$$

The behaviour of longitudinal magnetization recovery M_z is depicted in Figure 2.2 (left).
The transverse relaxation is the mechanism which results in a decay or decrease of the transverse magnetization, M_{xy}. The protons become out of phase again by exchanging energy with the surrounding protons, a **spin-spin interaction**. This loss of phase, following the application of a 90° pulse, is characterized by Equation 2.5.

$$M_{xy}(t) = M_{xy}^0 e^{-t/T_2} \tag{2.5}$$

,where T_2 is the transverse relaxation time constant, generally much shorter than T_1. The behaviour of recovery M_{xy} is depicted in Figure 2.2 (right).
The transverse relaxation time constant, T_2 relaxation, also depends on fluctuations of the z-component and consequently T_2 is always less or equal to T_1.

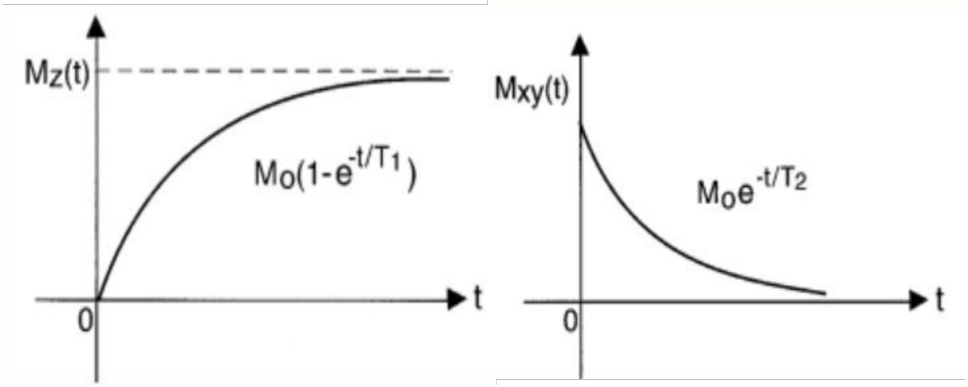

Figure 2.2: Longitudinal (left) and transverse(right) relaxation times, Adapted from [24].

However, in any real MR experiment, the transverse magnetization decays faster than what would be predicted by natural atomic and molecular mechanisms. This decay rate is commonly denoted as T_2^* ("T_2-star"). T_2^* can be considered an "observed" or "effective" T_2, whereas the first T_2 can be considered the "natural" or "true" T_2 of the tissue being imaged. T_2^* is always less than or equal to T_2. T_2^* relaxation refers to the decay of transverse magnetization, M_{xy} caused by a combination of spin-spin relaxation and magnetic field inhomogeneity. Typically these field inhomogeneities are removed by the application of a 180°, but some MRI techniques make use of this decay for T_2^* imaging, as shown in Figure 2.3 [25].

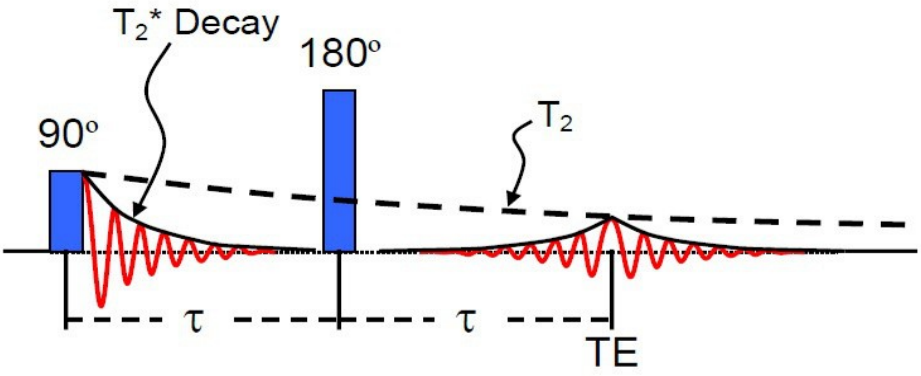

Figure 2.3: Echoes and echo time. Echo formation with a combination of a 90º and 180º RF pulses. Adapted from [26].

In summary, in the decay of the transverse magnetization two factors contribute to the loss of phase coherence: the natural loss of phase coherence and the B_0 inhomogeneities, respectively the "true" T_2 and T_2', respectively. The combination of both factors results in the transverse magnetization decay which is governed by the constant T_2^* given by

$$\frac{1}{T_2^*} = \frac{1}{T_2} + \frac{1}{T_2'} \tag{2.6}$$

The ease with which the adjacent atoms can absorb the surplus energy depends on the exact nature of the tissue and its physiological characteristics, allowing the differentiating tissue types. In other words, relaxation is the key to provide tissue contrast in MRI.

2.2 Imaging Principles

Nuclear Magnetic Resonance was a technique mainly used for spectroscopy, to study the chemical properties of materials and samples. In 1973, P. Lauterbur introduced the concept of spatial encoding using magnetic field gradients and added it to NMR which made MRI possible [27]. A. Kumar then used the magnetic gradients to obtain 2D Fourier encoded images [28], and P. Mansfield, following the developed work, acquired the first *in vivo* MR images [29].

The described works led to a new medical imaging technique - Magnetic Resonance Imaging (MRI). In other words, the MR signal originates from the induction of a small electrical current in the receiver coil by the precession of the net magnetization during resonance. This is a manifestation of Faraday's Induction Law, where a changing magnetic field induces a voltage in the nearby conductor. The time-dependent force induced in the RF coil by the change in magnetization in the M_{xy} plane carries the NMR information where every spin's contribution to the free induction decay (FID) is dependent on its location. In the following sections, the basic imaging principles, involving the processes taking place in the generation of the final MRI signal, are introduced.

2.2.1 Slice selection

In 2D-MRI, first a plane of interest in the body is selected for imaging. Knowing that the Larmor frequency of the protons is directly proportional to the applied steady external magnetic field B_0, it is possible to excite only a specific region of the total imaging volume. Equation 2.2 expresses this relationship, where w_L can be replaced by $2\pi f_L$, in order to lie within in the radio-frequency range.

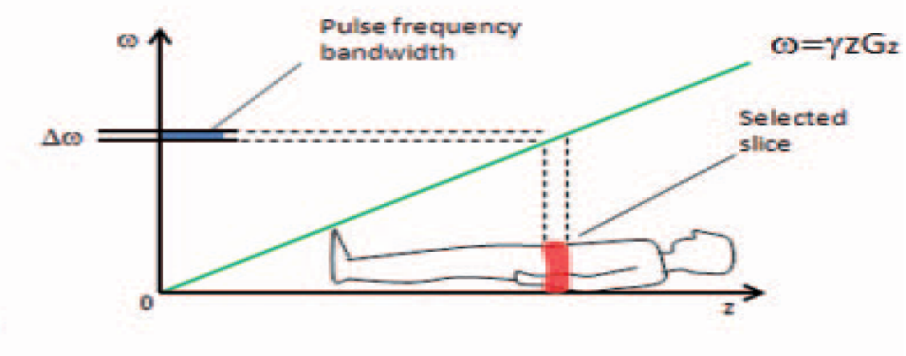

Figure 2.4: Slice excitation and relation between excited frequencies and slice thickness. Adapted from [30].

In other words, by changing the resonating frequecny in the corresponding section of the body, the protons in this area will resonance at a different frequency. If we apply a RF pulse of this specific frequency, only these protons in the regions will resonate, thus providing a way to identify the slice of interest.

The slice selection involves, then, a localized variation in the value of the external field, which is achieved by the usage of gradient field coils. By applying a linear magnetic field in the direction of choice, normally z, the amplitude of the magnetic field would vary in this direction. In more detail, two steps are required to uniquely excite a slice. Firstly, a slice-select gradient (G_z) is imposed along an axis perpen-

dicular to the plane of the desired slice, normally z, resulting in a linear variation of potential resonance frequencies in that direction. Secondly, a specially tailored RF-pulse is simultaneously applied, whose frequency components match the narrow range of frequencies contained in the desired slice. The narrow range of frequencies is defined by the position of the slice (z) and its thickness (Δz), which correspond, respectively, to the central frequency (F_c) calculated by Equation 2.7 and the range of frequencies around it, Δw, calculated similarly by replacing F_c with Δf and z with Δz.

$$F_c = \gamma(B_0 + zG_z) \tag{2.7}$$

The combination of both steps ensures that only protons within the chosen slice are excited.

2.2.2 Frequency and Phase encoding

Slice selection does not differentiate between protons within each slice. Two additional gradients are usually applied in order to encode the spins in the slice.
The measured slide is composed of a number of x columns and y rows, adding up to a total of x·y individual elements, called pixels.

One of the gradient fields establishes a specific frequency for one of the other remaining coordinates, usually the x-axis, similarly to the slice selection gradient. This gradient is commonly referred to as the **frequency encoding grading**, G_x. The other gradient modifies the phase of the precessing protons, in the remaining direction, the y-axis. This gradient is typically referred to as the **phase encoding gradient**, G_y. Both gradients have identical properties, but are applied in different directions, at different times. However, one must bear in mind that the x- and y-gradients do not skew or shear the main field transversely. They simply provide augmentation in the z-direction to the B_0 field as a function of anterior-posterior location in the gantry. The x- and y-gradients (ideally, at least) do not produce components perpendicular to B_0.

With the 3 gradients (G_x, G_y, G_z), the pixels can now be localized in all three directions (x, y, z). Other properties of the MR also aid in the localization of the MR signal, for example the differences in signal timing and the distance to the receiver coils. The adequate usage of this imaging strategies allows the acquisition of faster and better MRI images.

2.2.3 K-space and Image Reconstruction

The concept of k-space was first applied in magnetic resonance imaging in 1983 by Ljunggren [31] and Twieg [32].

As described previously, the MR signal results from current induction by precession of the net magnetization after excitation through an RF-pulse. The signal is detected by the receiver coils and can be represented by a vector with both real (Re) and imaginary (Im) components, or alternatively represented as a complex number like in Equation 2.8.

$$Signal = Re + iIm \tag{2.8}$$

, which through simply trigonometry correlates with the magnitude and phase of the signal detected by the following equations:

$$Mag = \sqrt{Re^2 + Im^2} \qquad \Phi = tan^{-1}\left(\frac{Im}{Re}\right) \tag{2.9}$$

The changes in the signal are stored in a temporal matrix, referred to as the k-space which codifies the image in frequency domain, rather than time domain. By applying a Fourier Transform (FT) on the k-space, the image reconstruction can be performed. To put it in simpler terms, the k-space can be defined as the space of spatial frequencies and is the inverse space of the physical coordinates system (x, y). The spatial frequency variables k_x and k_y are related to the time on gradient variables. Therefore, k-space data is just the MRI time domain data where the variables (t, (Gx,Gy, Gz)) were replaced by (k_x, k_y) [32].

The data to fill the k-space can be acquired in any order. While the Cartesian methods used to be the most dominant, nowadays, spiral or radially oriented trajectories are also widely used [33], [34].

2.3 Instrumentation and Equipment

An MRI scanner is made up of four main components: the magnet, the gradient coils, the radio-frequency coils (transmitter and receiver), and the computer. In this section the general design and main functions of these components are discussed, with the exception of the computer as its functions are obvious: operator interface, in addition to data storage and processing.

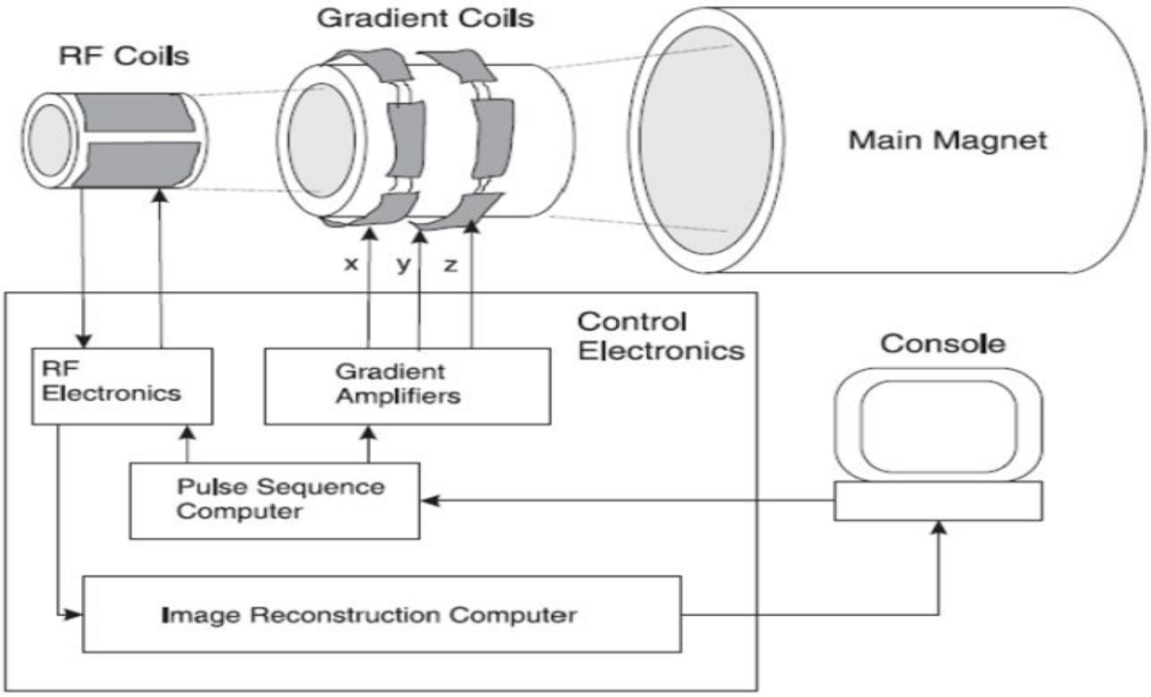

Figure 2.5: Schematic representation of the main components in a MRI system. Adapted from [35].

2.3.1 Magnet

Perhaps the most important component of the MRI scanner, the magnet, is responsible for generating the main static field, B_0 while assuring its homogeneity. The strength of the magnet is measured in teslas, T. Clinical magnets generally have a field strength in the range 0.1–3.0 T, with research systems available up to 9.4 T for human use and 21 T for animal systems.

The magnet can be categorized in three types of magnets: permanent, resistive or superconducting magnets. The first two were used in early MR experiments at lower fields. Permanent magnets are generally made from ferromagnetic materials and can only provide low field strengths (usually less than 0.4 T). Though very inexpensive to maintain, they cannot be switched off and they are of limited precision and stability. Resistive magnets are made of cheaper materials and generate magnetic fields of medium strength, but involve higher maintenance costs since they dissipate a lot of energy.

Nowadays, due to the need of higher field strengths, superconducting magnets are widely preferred. These magnets are generally made of a niobium-titanium alloy which is cooled to even inferior values than its critical temperature with liquid helium (around 10K) in order to, constantly, offer zero electrical resistance. Consequently, these magnets need to be refilled with helium at frequent time periods. An electromagnet constructed with superconductors can have extremely high field strengths and with very high stability, causing them to be the most sought after.

When the MR scanner is placed in the hospital or clinic, its main magnetic field is far from being homogeneous enough to be used for scanning. The shim coils are a set of resistive coils which are placed inside the magnet and are able to produce field corrections.

2.3.2 Gradient Coils

As referred in Section 2.2.2, gradient coils are responsible for spatially encoding the position of the protons by varying the magnetic field linearly across the imaging volume. Gradient coils are usually resistive electromagnets powered by sophisticated amplifiers which permit rapid and precise adjustments to their field strength and direction. When an electrical current passes through these coils, the main magnetic field is focally distorted in certain places, creating the desired magnetic field changes.

The performance of the coils is dependent on the gradient strength, linearity, stability, duty cycle and slew rate times. The slew rate of a gradient system is a measure of how quickly the gradients can be ramped on or off. In parallel, the performance of the gradient coils influences the sequence design and scanning time as stronger gradients allow for faster imaging, and, similarly, gradient systems capable of faster switching can also permit faster scanning. However, gradient performance is limited by safety concerns over nerve stimulation.

2.3.3 RF Coils

The RF coils generate (transmitter coil) RF pulses and detect (receiver coil) the generated signals essential to the MRI signal's generation. There is a saying in MRI that goes : "An MR scanner is a coil within a coil within a coil within a coil...". Although ironic, there is some ground truth in this saying. Apart from the main magnet and gradient coils, there are also the RF body coil and the patient coils. The

body coil is responsible for transmitting (and can also receive) the B_1 field, while the patient coils, for example the head coil, lay closer to the imaged region in order to better receive the signal and increase its quality. These patient coils can also be referred to as surface coils, as they can be made with different shapes to better contour the body region which is being imaged.

2.4 MR Sequences

2.4.1 Spin-Echo (SE)

A single radio-frequency pulse generates a free induction decay, however, if another RF pulse is applied, which refocuses the excited spins, spin echo signals can be produced. In a slice-selective spin-echo (SE) sequence, the first excitation pulse of 90° is applied together with a slice selection gradient to tip the proton spins into the transverse plane. Since not all spin groups are equal, local microscopic fields may differ causing some spin groups to gain phase and precess faster. After the RF excitation, a phase gradient is applied along the y-axis, whose amplitude determines the y-line of the k-space to be filled. The 180° RF pulse is then applied together with the same slice selection gradient to flip the spins and make them rotate back towards coherence. The signal is acquired around echo time (TE), while a readout gradient along the x-axis is switched on. A schematic overview of a SE sequence is illustrated in Figure 2.6.

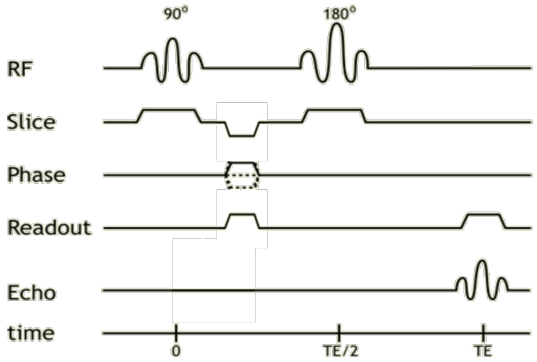

Figure 2.6: Schematic of a 2D SE MR sequence. A 90° pulse is applied for excitation. At TE/2 a refocusing 180° pulse is applied and at TE the signal is acquired. Adapted from [29].

2.4.2 Gradient-Echo (GE)

As the name implies, in a gradient-echo (GE) sequence, gradients are used to dephase and rephase the transverse magnetization vector instead of the 180° RF pulse. In GE sequence, an RF pulse is applied to partially flip the net magnetization vector into the transverse plane (flip-angle-α). The first gradient is applied to dephase and then a gradient with opposite sign is applied with the same strength but opposite polarity to the dephasing gradient, to rephase the spins.

A slice-selective GE sequence begins with the application of a RF excitation pulse simultaneously with the slice selection gradient. When the excitation pulse is turned off, the protons begin to dephase and a phase encoding gradient is applied along the y-axis. Simultaneously or instantly after, a negative readout gradient is applied along the x direction in order to induce a faster dephasing of the protons. Thereafter, a positive readout gradient is applied to rephase the protons at the same time as the echo is measured. A

schematic overview of a GE sequence is illustrated in Figure 2.7.

Furthermore, in a GE sequence, as the refocusing of spins are purely based on gradients and not on a 180° pulse, the local field inhomogeneities, due to susceptibility effects, are not compensated by the echo. Therefore, the signal is dependent of T_2^* rather than T_2 which leads to T_2^* -weighted images instead of T_2-weighted images in the SE sequence.

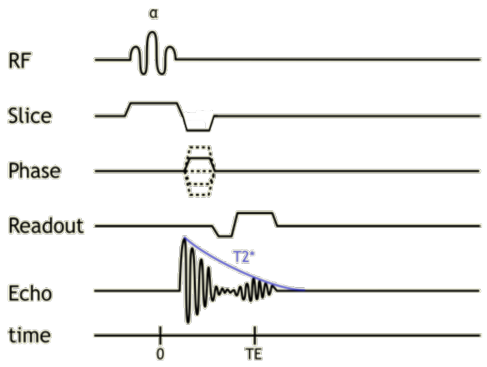

Figure 2.7: Schematic of 2D GE MR sequence. Following the RF excitation pulse, a phase gradient is applied. Immediately after, a negative readout gradient is applied for faster proton dephasing, followed by a positive readout to rephase the protons again, while echo is measured. Adapted from [29].

2.4.3 Echo-Planar Imaging (EPI)

Advances in gradient and digital data acquisition technology have made it possible to obtain individual MR slices in the time frame of 50-100 msec, thus minimizing the effects of patient motion, while aiming to increase temporal resolution. Generally, the used imaging technique is called echo-planar imaging, EPI. Although EPI seems to be a rather recent technique, it is one of the oldest as it was first described by Mansfield in 1977 [29]. However, this technique was prone to severe image distortions. As originally defined, EPI referred to a sequence in which data from all of k-space for an entire 2D plane was collected following a single RF-excitation pulse. More recently the term has been expanded to include any rapid gradient-echo or spin-echo sequence in which k-space is traversed in one or a small number of excitations. In the modern lexicon, these are termed single-shot EPI and multi-shot EPI, respectively.

EPI is an imaging technique where an RF pulse is followed by a strong frequency encoding gradient applied simultaneously with an intermittent low magnitude phase encoding gradient. A schematic overview of a EPI sequence is illustrated in Figure 2.8.

An EPI pulse sequence differs from conventional pulse sequences as EPI employs a series of bipolar readout gradients to generate a train of gradient echoes. With an accompanying phase-encoding gradient, each gradient is distinctively spatially encoded so that multiple k-space lines can be sampled under the envelope of a FID or an RF spin echo. EPI uses a gradient-echo train to accelerate data acquisition, generating images in a considerably shorter time.

This leads to a k-space sparsely filled in with a trajectory represented on Figure 2.9.

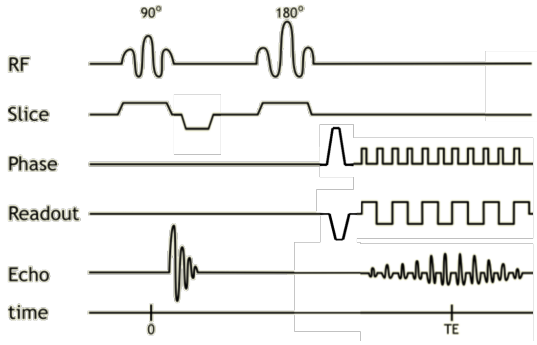

Figure 2.8: Schematic of a 2D EPI MR sequence. An RF pulse is followed by a strong frequency encoding gradient applied simultaneously with an intermittent low magnitude phase encoding gradient. The data is acquired from [29].

2.4.3.1 Single-shot and Multi-Echo EPI

Regarding the k-space sampling, EPI sequences can be divided into two groups: Single-Shot and Multi-Shot or also named segmented. The main difference between both sequences is on the k-space acquisition.

In a single-shot sequence, the entire range of phase encoding steps are acquired [36]. Therefore, the all k-space data are acquired in only one shot, achieved by generating and reading all of the required echoes from a single FID as shown in Figure 2.9. However, the image acquisition matrix is typically no larger than 78x78. Nowadays, single-shot EPI is the most widely available fast imaging sequence on clinical scanners and facilitates whole-brain coverage at reasonable Signal to Noise Ratio (SNR). Single-shot can easily be applicable because it does not need specialized gradient amplifiers to perform the required gradient switching.

In multi-shot sequence, more excitations are needed to acquire the information of one slice. Also, the range of phase encoding steps is equally divided into several "shots" per slice. Thereby, a subset of readout gradient is acquired within each TR and the k-space is acquired in each shot. The shots are repeated until a full set of data is collected as illustrated in Figure 2.9. This sequence can be applied in diffusion and perfusion MRI due to the requirement of shorter TE [36].

When comparing multi-shot EPI with single-shot EPI, the first one is less prone to image distortions [37]. Recent studies have shown that physiological noise originated from respiration increase linearly as the number of shots increase for a fixed TR in a multi-shot EPI [38].

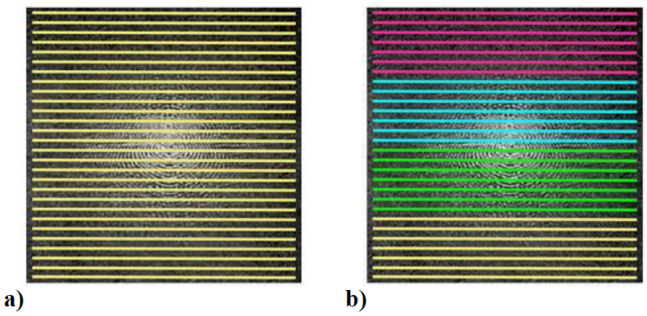

Figure 2.9: K-space acquisition for a) single-shot b) multi-shot. Adapted from [39].

Comparisons between single-shot and multi-shot EPI reported that in multi-shot, the SNR is higher than in single-shot due to the shorter TE and presents less susceptibility artifacts due to shorter readouts. However, this sequence requires longer TR when compared to single-shot for the same number of slices and resolution [36].

2.4.3.2 Echo-Planar Imaging with Keyhole (EPIK)

In 1993, several researchers from the Netherlands, proposed using a keyhole method for accelerating imaging of contrast agent uptake, where one would skip the acquisition of the data normally taken with strong phase-encoding gradients [39]. This imaging method was proven to be compatible with other acceleration methods and Shah et al. suggested that when combined with EPI, perhaps the resulting images would not wield as many distortions. This originated a theoretical EPIK that was then validated at 1.5 T, for 3 T and fMRI [40]. Furthermore, this method, when compared to EPI, showed, not only a higher temporal resolution and smaller image distortions, but also enhanced characterization of functional areas [41].

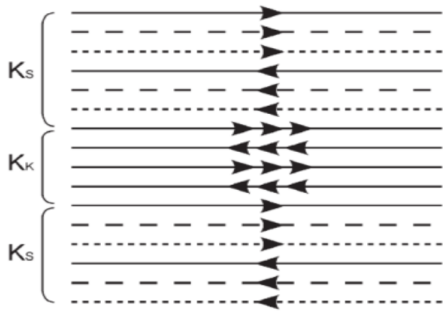

Figure 2.10: K-space acquisition for EPIK. Each k-space trajectory is devided intro three distinct regions: a keyhole region (K_k) where the all lines are sampled in every measurement; and two sparse regions (K_s) where each measurement acquires only certain lines. Adapted from [16].

EPIK consists of a multi-shot EPI sequence where keyhole technique is applied. Keyhole techniques are based on the principle that the information in the high spatial frequencies is relatively little, therefore

only the low frequencies of an area of the k-space are updated. However, EPIK is not a standard keyhole technique. In EPIK, the periphery of the k-space, containing high spatial resolution information, is continually updated, although more sparsely as illustrated in Figure 2.10. When compared with EPI, with the sharing of the k-space, EPIK acquisition times are shorter, maintaining similar SNR, reducing susceptibility artifacts and improving spatial resolution.

2.4.4 Look-locker based T_1 mapping sequence

Quantitative measurement of T_1 relaxation time is of great importance in many applications as its knowledge can be used for the diagnosis of human brain diseases or for optimizing image's contrast. The traditional "gold standard" method used for determining tissue T_1 was to perform a series of independent single-point inversion recovery signal measurements at different TI's. In 1970, Look and Locker reasoned that instead of making a single measurement at a fixed TI after inversion, many more data points could be acquired by sampling a periodic train of rapidly applied constant flip-angle pulses. Rather than being only one sequence, Look-locker is a method, from which several sequences have been developed.

Echo-planar imaging was incorporated into the inversion recovery LL-based method by interleaving EPI readouts for eight different slices after an inversion pulse [42]. The sequence was repeated and the slice order was changed to achieve a range of inversion times for each slice, in a total acquisition time of thirty seconds [43]. More recently, a LL-based method using EPIK was proposed [44]. A sequence scheme of this method can be seen in Figure 2.11.

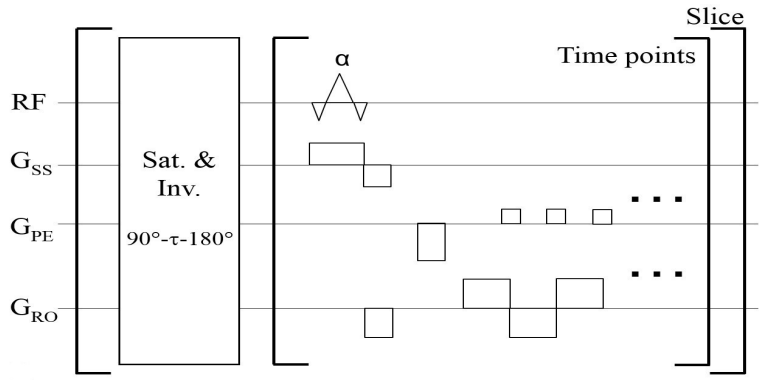

Figure 2.11: Sequence diagram of the Look-Locker method using EPIK. Before the first inversion pulse and data acquisition, a series of ° preparation pulses are applied to make the longitudinal magnetization in each imaging plane approach a steady state.Adapted from [44].

2.4.5 SAGE-EPI or GESE-EPI

In order to overcome and address some of the associated drawbacks of gradient-echo and spin-echo sequences, several methods were proposed to combine gradient-echo with spin-echo, echo planar imaging [17]. These new pulse sequences facilitated the simultaneous acquisition of GE and SE data [45]. However, the MRI pulses sequences used in [17], [45] and [46] have the drawback that they are all sensitive to T_1-shortening effects caused by CA extravasation through the bloodstream. Also, in some previous studies few echo trains prevented the absolute quantification of R_2 and R_2^* [45].

With the purpose of overcoming the limitations on the existing sequences that tried to combine SE and GE, a spin- and gradient-echo echo-planar imaging (SAGE-EPI) MRI pulse sequence was created [17] also referred as GESE-EPI. In SAGE, a spectral–spatial signal excitation pulse is followed by two EPI readout trains acquired at echo times TE_1 and TE_2, a 180° refocusing pulse, and three more EPI readouts (TE_3–TE_5), with the last readout at TE_5= TE_{SE} resulting in a SE signal.

The SAGE-EPI pulse sequence is similar to the multi-echo PERMEATE (perfusion with multiple echoes and temporal enhancement) sequence described previously in [16], extended by a 180° refocusing pulse and additional EPI readout trains to measure both GE and SE data.

A schematic overview of a SAGE sequence is illustrated in Figure 2.12.

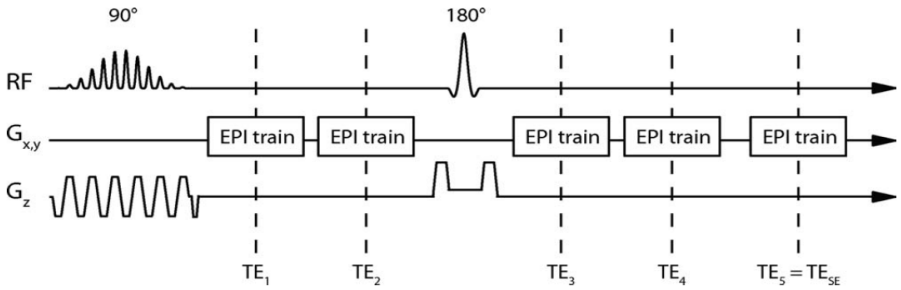

Figure 2.12: Schematic representation of SAGE EPI sequence. After a 90° excitation pulse, two gradient-echo are applied each at a certain TE. A 180° refocusing pulse is then applied, followed by two more gradient-echos and the final spin-echo. Adapted from [17].

2.4.5.1 SAGE EPIK or GESE EPIK

However, the SAGE-EPI approach also has the usual limitations such as susceptibility artefacts and geometric distortions resulting from the single-shot EPI readout. Therefore, an alternative method for GESE-EPI using EPIK was proposed in [53]. This method showed improvements in the perfusion measurements, having a reasonable trade-off between spatial/temporal resolution and brain coverage. SAGE-EPIK maintains the same sequence design as SAGE-EPI. The only difference is the applications of the Keyhole technique with and interleaved sampling multi-shot EPI. Instead of using EPI trains to generate the gradient echoes, EPIK trains are applied, taking advantage of the benefits of keyhole technique, as shown in Figure 2.13.

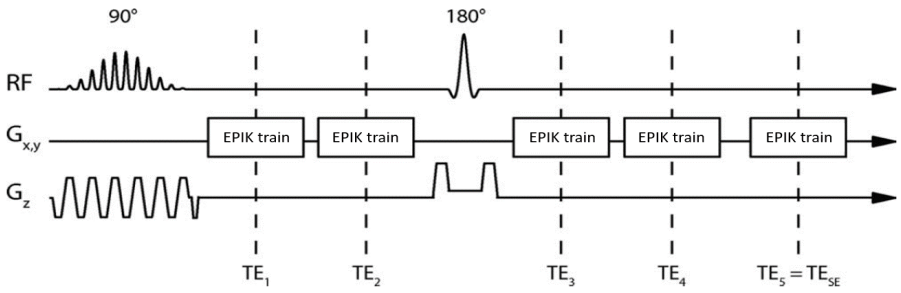

Figure 2.13: Schematic representation of SAGE EPIK sequence. Similarly to SAGE EPI with the difference of taking advantage of keyhole technique. Adapted from [17].

2.5 Hybrid Imaging

Historically, medical devices, used to image either anatomical structure or functional processes, have been developed somewhat along independent paths. CT, PET and MRI are the main techniques used in brain studies. CT provides anatomical information, PET provides functional/metabolic information, meanwhile MRI provides anatomical and functional/metabolic information. However, the recognition that combining images from different techniques can nevertheless offer significant diagnostic advantages gave rise to hybrid imaging techniques.

Hybrid imaging is a term used to refer to the combination of two, or more, imaging modalities to form a new technique, in order to overcome some of the existing drawbacks of the individual modalities. MR-PET is a example of this combination, and was used in this study, therefore further information is given in the following subsection.

2.5.1 MR-PET

MRI is a imaging technique that has been deeply described throughout this chapter, both in terms of the theoretical principles behind it and mainly used hardware, but different sequence schemes were also approached.

Positron-emission tomography (PET) is, very briefly, a powerful nuclear medicine imaging technique that can be used to measure metabolic activity or body function processes *in vivo*. The system detects pairs of gamma rays emitted indirectly by a positron-emitting radionuclide, which is introduced into the body on a biologically active molecule called a radioactive tracer and decays throughout time. Three-dimensional images of tracer concentration within the body are then constructed by computer analysis. In summary, PET imaging provides information about tracer uptake revealing information about the tumor activity.

Each of these imaging procedures, has its own advantages and drawbacks. Combining imaging modalities to use their strengths together and to compensate for their weaknesses has been a major asset in combined modalities. For these reasons, and following the success of combined PET-CT, in recent years, several research groups have re-addressed the applications of and developed combined PET-MRI systems. To be of notice that the first PET-MR devices were built even before the introduction of PET-CT

[47][48]. However, several technical difficulties made the combination of these two modalities challenging and the first integrated system study of the human brain was only published in 2008 [49].

For brain studies, the combination of MR and PET addressed some of the existing limitations of each technique in addition to improving pathologies' diagnostic. While MR imaging allows the differentiation between healthy and unhealthy tissues in most brain regions with normal cells, PET has the unique capability of directly showing metabolism to a cellular level resultant from tracing the tracer uptake. Hereupon, by combining both techniques more information can be easily assessed comparing with MRI and PET standalone instruments.

Chapter 3

Brain Tumors

A brain tumor consists of a tissue mass formed by an abnormal growth of brain cells. A healthy cell usually ages and eventually dies, being replaced by an equal one. However, sometimes these cells mutate and the organism is not able to remove them, allowing them to grow and replicate, forming what is considered as a tumor mass. These mutated cells function differently from the normal cells. If a brain tumor is composed of neuroglia cells and fibers, it is called a glioma. These cells provide support to the neurons and are responsible for their protection and nutrition. 30% of all brain tumors are gliomas.

There are mainly two types of tumors: benign and malignant tumors. Benign tumors are typically localized, not invading nearby tissue, and do not spread to other parts of the body. Usually these tumors respond well to treatment. Malignant tumors, however, have infiltrated the nearby tissue, are often resistant to treatment, may spread to other parts of the body and sometimes recur after being removed [50].

As a tumor grows to a few mm^3 in volume, it will reach a point in time where it can no longer rely on the passive diffusion of metabolites from the blood vessels to continue its development [51]. For that new blood vessels must be generated in a process known as angiogenesis [52]. These newly developed vessels are, in comparison with mature blood vessels, leaky, fragile and incompletely formed. These differences can be exploited to indirectly characterize the state and grade of the tumor.

Several studies, are also investigating if the tumors can change the brain-blood barrier (BBB) integrity and functionality [53]. The BBB is a highly selective semipermeable membrane barrier that separates the circulating blood from the brain and extracellular fluid in the Central Nervous System (CNS). This barrier allows the passage of water, some gases and other molecules crucial to neural function, while preventing the entry of harmful substances. Despite what was first believed, tumors only change the integrity of the BBB, not its functionality.

For CNS tumors, perfusion MRI techniques are more used since they allow quantification of specific parameters and more accurate tumor grading and differentiation between healthy and tumor tissue.

3.1 Classification and Grading

Over the past century, tumor classification has been mainly performed according to the tumor histology. In other words, tumors are classified depending on its microscopic features such as vascularization, presence of certain proteins, etc. Studies over the past two decades have clarified that other factors should be taken into consideration when grading the tumor, such as tumor genetics, prognostic to treatment, tumor anatomic structure, among others ([7], [8], [9], [54]).

In pathology, grading tumor is a matter of how different from the original healthy tissue, the tumor tissue appears. According to the classification of the World Health Organization (WHO), it is possible to grade the gliomas on a scale from I to IV, being I the lowest grade and IV the highest. Grade I and II are associated with low malignancy rate, and are often referred to as low grade gliomas (LGG). Analogously, grade III and IV refer to higher malignancy, being often addressed as high grade gliomas (HGG) [55].

The diagnosis, grading and classification of tumors has benefited considerably from the development of MRI which is now essential to the adequate clinical management of many tumor types. The ability of MRI to not only image the tumor but also demonstrate its morphology and the relationships of malignant lesions to neighboring structures provide essential medical information. When referring to brain tumors, conventional MRI is able to provide detailed anatomic images of the CNS tumor. However, grading and evaluating the malignant potential of a CNS tumor with conventional MRI has been less successful, in particular, due to factors such as T_1 and T_2 relaxation times, related to tumor angiogenesis and the integrity of the blood-brain barrier of neoplastic tissue, being only moderately specific indicators of malignancy. Meanwhile, PET using biologically active molecules labelled with short-lived positron-emitting isotopes at micromolar or nanomolar concentrations is one of the most promising techniques for the imaging of specific molecular processes *in vivo*. Molecular imaging using PET may provide relevant additional information on tumour metabolism, and may also be helpful in clinical decision-making, especially in patients with equivocal MRI findings. In particular, the clinical value of ^{18}F-FET PET for the identification of tumour relapse has been demonstrated in numerous studies including patients with gliomas as well as patients with brain metastasis [56], [57], [58].

Chapter 4

Perfusion MRI

The delivery of oxygen and nutrients to the tissue by means of blood flow is commonly known as perfusion.

Perfusion MRI is a term used to refer to a variety of MRI techniques that give insight on the parameters of cerebral microvascularization: regional blood volume, mean transit time, regional blood flow, etc. The ability of perfusion MRI to provide information on these parameters has led to these sequences being used routinely for an increasing number of indications, including tumor imaging, cerebrovascular disease and more. Therefore, the development of acquisition methods with higher resolution, higher speed and less artifacts is of interest for the all medical community [59].

Perfusion MRI works around the Fick's Principle, which derives from the conservation of mass, and states that the blood flow, BF, to an organ can be calculated using a marker substance if we know the concentration of the marker taken by the organ, $C_T(t)$, the concentration in the arterial blood supplying the organ, $C_A(t)$, and the concentration in the venous blood leaving the organ, $C_V(t)$. The Fick's Principle can be represented by Equation 4.1.

$$\frac{dC_T(t)}{dt} = BF \cdot [C_A(t) - C_V(t)] \tag{4.1}$$

Perfusion MRI techniques are classified on whether they involve the usage of an exogenous contrast or not. On one hand, bolus methods, like DSC and DCE, with injection of a contrast agent, provide better sensitivity with higher spatial resolution and are more widely used in clinical applications. On the other hand, Arterial Spin Labeling methods allow a completely non-invasive measurement of blood flow while exploiting an endogenous contrast and have better accuracy for quantification. The difference between the two first techniques relies on the evaluation of T_1 changes, the so-called dynamic contrast enhancement (DCE), or to observe changes in T_2 and T_2^* susceptibility due to paramagnetic Gd^{3+} ions, the so-called dynamic susceptibility contrast (DSC). Because the purpose of this work focuses around these two last techniques, they are described in more detail in the following sections.

4.1 DSC-MRI

Dynamic susceptibility contrast MRI (DSC) is one of the exogenous contrast perfusion imaging methods. It relies on the injection of a paramagnetic contrast agent, typically Gadolinium-based accompanied by rapid measurement, using fast imaging techniques, of the transient signal changes during the passage of the bolus through the brain-also known as *Bolus Tracking*.

4.1.1 DSC-MRI Data Acquisition

In a typical DSC-MRI imaging session, especially in tumor studies, a *preload* injection of about a quarter of the contrast agent is administered to reduce T_1 leakage effects on the actual measurements. After a short period of time, around 5 minutes, the rest of the contrast agent is injected and rapid T_2- or T_2^*-weighted images are obtained over the entire brain or a section of it. The standard sequence used in DSC is the single echo, single shot EPI due to its fast temporal resolution.

After the contrast agent's injection, the hemodynamic signal of DSC will depend on the T_2 and T_2* relaxation times. The contrast agent will mainly stay within the vascular space and, as the CA is a paramagnetic material, it will distort the magnetic field and reduce T_2 around the vessels due to an increased susceptibility effect. This reduction can be explained by Equation 4.2, keeping in mind that T_2=1/R_2, T_2^*=1/R_2^* .

$$(R_2^* = R_{20}^* + r_2^* \cdot C_b) \tag{4.2}$$

, where R_{20}^* is the intrinsic gradient-echo transverse relaxation rate on the brain tissue without the contrast agent, r_2^* is the transverse relaxivity of the contrast agent, which depends on the blood volume and vascular morphology, and C_b is the intravascular blood concentration of the contrast agent. This relationship can also be applied in a spin-echo sequence as:

$$R_2 = R_{20} + r_2 \cdot C_b \tag{4.3}$$

The signal S measured over time t from DSC using a gradient echo-based sequence can be described by:

$$S(t) = M_0 sin(\alpha) \cdot \left[\frac{1 - e^{\left(-\frac{TR}{T_1(t)}\right)}}{1 - cos(\alpha) \cdot e^{\left(-\frac{TR}{T_1(t)}\right)}} \right] \cdot e^{\left(-\frac{TE}{T_2*(t)}\right)} \tag{4.4}$$

,where M_0 is proportional to the equilibrium magnetization and α is the flip angle used in imaging. In order to measure the changes that occur in T_2^* , all acquired data are compared to a baseline signal at time t=0. Considering that the T_1 changes are small within tissue, Equation 4.4 can be simplified to

$$\Delta R_2^* = \frac{-1}{TE} ln \left(\frac{S_B}{S(t)} \right) \tag{4.5}$$

, where S_B represents the signal from the baseline. This corresponds to a time interval where there is no contrast agent detection, yet. Lastly, the most technically demanding portion of the acquisition process in DSC-MRI is acquiring an estimate concentration of the contrast agent in the blood plasma as a function of time, $C_p(t)$, the AIF. This function is required to perform nearly all currently available

analysis methods. The AIF can be estimated in three different ways. One approach involves introducing an arterial catheter into the subject and sampling blood during the scanning process for later analysis [60]. A second method assumes that the AIF is similar for all subjects and averages some AIF's from previous subjects to generate an averaged AIF usable for all subsequent studies [61]. A third method obtains the AIF from the MRI data-sets themselves [62].

4.1.1.1 DSC-MRI Data Analysis

With all acquired data, DSC-MRI parameters can now be estimated. The T_2 and the T_2^* changes measured through the acquisition time can be assessed in two different ways: a direct analysis of the signal curves originated from each voxel through time, or full quantification of the contrast agents concentration change and fitting of the data to a kinetic model in order to derive quantifying parameters. Each method has its disadvantages and advantages and must be picked according to the study's objective.

4.1.1.2 Non-parametric Approaches

With few, or even, any computational analysis, it is possible to extract semi-quantitative perfusion parameters from the intensity curve of the acquired signal data. These parameters are relatively easy to calculate and useful when fast and no in-depth analysis is required. However, this analysis is not very precise and lacks consistency. Some semi-quantitative DSC-MRI perfusion parameters are represented in Figure 4.1 and defined in Table 4.1.

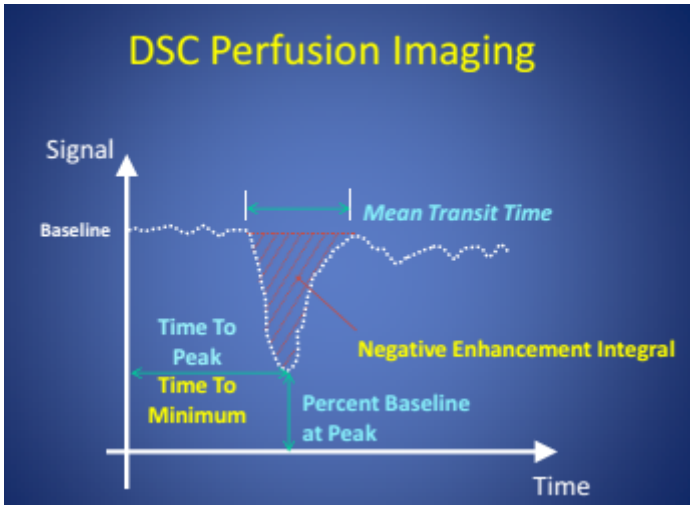

Figure 4.1: DSC-MRI signal curve with representation of semi-quantitative perfusion parameters. Adapted from [63].

Table 4.1: Nonparametric values of DSC-MRI.

AT or T_0	**Arrival Time** is the first interval between intravenous contrast injection and its first detection in tissue or a large artery.
TTP	**Time to Peak** corresponds to the time the intensity curve takes to reach its peak of signal loss within the organ of interest .
NEI or AUC	**Negative Enhancement Integral** or **Area Under the Curve** reflects the total amount of contrast transiting through the regional vascular system.
MTE	**Mean Transit to Enhance** reflects the average time for all injected contrast to pass through the tissue region.
PBP	**Percent Baseline at Peak** is the ratio between signal intensity at minimum peak with its baseline values.
PSR	**Percent Signal Recovery** is the ratio between signal intensity during the re-circulation phase with its baseline value.

4.1.1.3 Parametric Approaches

To fully quantify perfusion parameters, a kinetic model must be applied to explain the inherent physiology. The most accepted kinetic models used for perfusion quantification rely on the assumption that the contrast material remains within the vascular space as long as the brain-blood barrier remains intact and T_1 changes after injection are negligible [64]. The fraction of injected CA still present in a vasculature at t time is described by the **Residue function**, R(t).

$$R(t) = 1 - \int_0^t h(t)\,dt \tag{4.6}$$

, where h(t) represents the probability density function of transit times. By definition of h(t) as a probability density function, R(0) is equal to one and R(t) is a positive, decreasing function of time [65]. Consequently, the tissue contrast curve $C_t(t)$ is a relation between the arterial input function (AIF) and cerebral blood flow (CBF), as represented on

$$C_t(t) = CBF \cdot AIF(t) \otimes R(t) \tag{4.7}$$

Cerebral Blood Flow is an important parameter that evaluates the blood's ability to perfuse brain tissue adequately in a given time period, representing the instantaneous capillary flow in tissue.

The maximum of CBF · R(t) is usually considered to represent the actual blood flow to the tissue and can be estimated with knowledge of the AIF and application of the convolution theorem,

$$CBF \cdot R(t) = FT^{-1}\left[\frac{FT(C_t(t))}{FT(AIF(t))}\right] \tag{4.8}$$

, where FT^{-1} is an inverse of Fourier Transform.

An alternative approach is an algebraic reformulation, derived from the discrete convolution of Equation

4.7, where the data are sampled at equally spaced time intervals.

$$c = AIF\,(CBF \cdot r) \tag{4.9}$$

, where vector CBF · r contains the unknown discrete flow-scaled residue function.

To obtain the CBF, an alternative approach consists of treating the previous algebraic formulation as an inverse matrix problem and solve it using singular value decomposition (SVD). SVD decomposed AIF^{-1} into three matrices, $AIF^{-1}=VW^{-1}U^{T}$, where V and U are orthogonal and W is a diagonal matrix, whose inverse is therefore trivial. CBF is then computed from the maximum of:

$$CBF \cdot r = V \cdot \left[diag \frac{1}{w_j} \right] \cdot \left(U^T c \right) \tag{4.10}$$

, where w_j are the diagonal elements of W [66].

The Cerebral Blood Volume (CBV) is another important parameter defined as the volume of blood in a given amount of tissue, being proportional to the total amount of intravascular CA in the tissue. In order to obtain a normalized value, it is divided by the total amount of injected contrast

$$CBV = \frac{k_h}{\rho} \frac{\int_0^\infty C_t\,(t)\,dt}{\int_0^\infty C_a\,(t)\,dt} \tag{4.11}$$

, where k_h is a correction factor for the higher erythrocytes concentration in arterial blood than in capillary blood and ρ is the brain's density. This correction factor is only used when absolute quantification is required.

Finally, one last parameter can be calculated. The Mean Transit Time (MTT) is a measure of the main time for the blood or the contrast agent to perfuse a region of tissue. It is obtained by using the central volume theorem [64].

$$MTT = \frac{CBV}{CBF}. \tag{4.12}$$

4.2 DCE-MRI

It has long been of doctors' interest to acquire blood flow and blood vessels information in order to characterize and diagnose a pathology. In 1927 Egas Moniz introduced cerebral angiography using injection of a contrast agent combined with traditional radiography. This tool soon became a powerful imaging technique for the identification, characterization and localization of several medical conditions.

The crescent necessity for imaging techniques to characterize the angiogenic vasculature in drug development trials and to study of tumor biology, impulsed by the combination of MRI with angiography, lead to the establishment of DCE-MRI.

DCE-MRI is one of the exogenous contrast methods based on perfusion imaging methods. It refers to the acquisition and analysis of MRI data that describes the uptake of an intravenous contrast agent in regions of interest (ROIs), through evaluation of signal changes related to T_1 relaxation time.

4.2.1 DCE-MRI Data Acquisition

In a typical DCE-MRI imaging session, MR images are collected before, during and after CA injection into a vein. Each acquired image corresponds to one time point, and each pixel in each image set gives rise to its own time course which can then be analyzed. A typical DCE-MRI data acquisition requires three measurements:

1. Recording a map of the native T_1 values before contrast administration;
2. Acquisitions of T_1-weighted images following CA introduction at a reasonably high temporal resolution (10-30 second range) to be able to characterize the kinetics of the CA entry and exit into the tissue;
3. A method to estimate the time rate of change of the concentration of the CA in the blood plasma, the so-called arterial input function (AIF).

For the first measurement, there are several methods available but the most commonly used is a series of spoiled gradient-recalled echo images, acquired with different degrees of T_1-weighting. Equation 4.13 describes the measured signal intensity for such an image.

$$S(t) = M_0 \cdot \frac{sin(\alpha)[1 - e^{\left(-\frac{TR}{T_1(t)}\right)}]}{1 - cos(\alpha)e^{\left(-\frac{TR}{T_1(t)}\right)}} \cdot e^{\left(-\frac{TE}{T_2*(t)}\right)} \tag{4.13}$$

, where M_0 is a instrument scaling factor, α is the flip angle, TR is the repetition time and TE is the echo time. The idea is to acquire several images with different flip angles and fit the data to Equation 4.13 with M_0 and T_1 as floating parameters.

After the acquisition of the T_1-map, a series of heavily T_1-weighted images must be acquired as the contrast agent's is injected. To achieve these T_1-weighted images at such a rapid temporal resolution, compromises in the image quality or tissues range (number of slices) must be made. On the one hand, the images must be acquired with sufficient temporal resolution to characterize the CA enhancement characteristic of the tumor under investigation. On the other hand, the images must be acquired with high enough spatial resolution and coverage in order to image the whole lesion or tumor's inherent heterogeneity.

While designing a DCE-MRI data acquisition protocol, one needs to consider the goals of the study and carefully select the appropriate study parameters balancing the needs of the study with resolution issues. If a "semi-quantitative" analysis is planned and probing tumor heterogeneity is viewed as important, then spatial resolution is prioritized. If full quantitative analysis is needed and the CA kinetics need to be well sampled for accurate model fitting, then high temporal resolution is prioritized.

To satisfy all of these often-conflicted demands, DCE-MRI imaging protocol almost exclusively employs multi-slice 2D sequences that can be acquired rapidly while allowing for relatively high temporal signal to noise ratio and spatial resolution.

Similarly to DSC-MRI, perfusion DCE-MRI also requires the measurement or estimation of the AIF for full quantification of its perfusion parameters. The AIF for DCE can be acquired with the same methods described before in Section 4.1.1

4.2.2 DCE-MRI Data Analysis

With all needed data acquired, DCE-MRI parameters can now be estimated. Signal enhancement seen on the acquired T_1-weighted images can be assessed in two ways, as already referred: i) analysis of signal intensity changes which are so-called “semi-quantitative” or "non-parametric approaches" and ii) quantification of contrast medium concentration change using pharmacokinetic modeling techniques, which are so-called "quantitative" or "parametric" approaches. Semi-quantitative parameters describe tissue signal intensity enhancement using a number of descriptors [67]. Meanwhile, quantitative methods involve more rigorous theory and modeling and thus, in principle, more accurately reflect physiology than the semi-quantitative methods. However, quantitative methods, not only are technically more demanding, but may also not be as reproducible, repeatable, or robust to noise as semi-quantitative methods. With this and the goals of the study in mind, the proper analysis must be chosen. If only relative changes are required, then a semi-quantitative approach may suffice.

4.2.2.1 Non-parametric Approaches

The non-parametric dynamic perfusion analyses derive empirical indexes that characterize the shape and structure of the signal curve, S(t), giving some information related to the underlying physiology of the tissues. These methods are generally simple and less time consuming as they do not require many computational steps. In addition, the arterial input function, AIF, is also not required. However, as these analyses methods are directly based on the signal curve, the resulting information can be influenced by differences in MRI acquisitions parameters or/and scanner types. Although, as stated before, these methodologies cannot derive physiological information, e.g.vascular permeability and blood flow, directly from the S(t); there is a correlation between the curve-related measurements and the implicit system’s biology.

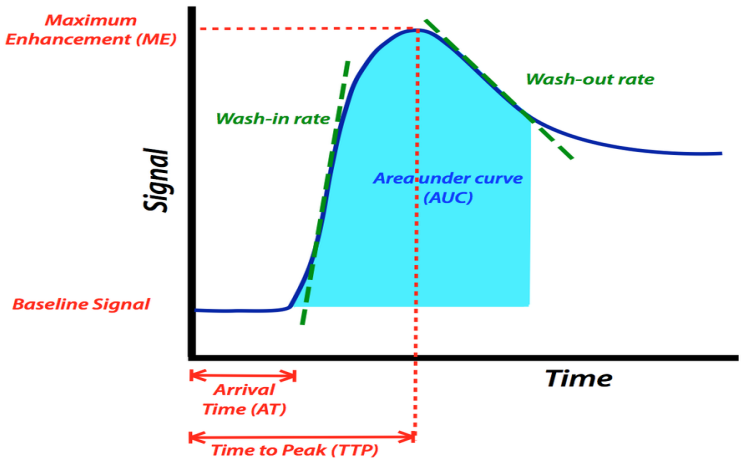

Figure 4.2: DCE-MRI signal curve with representation of semi-quantitative perfusion parameters. Adapted from [68].

These perfusion related measurements are defined in Table 4.2 and some are represented in Figure 4.2.

Table 4.2: Non-parametric values of DCE-MRI. Adapted from [69].

AT *or* T_0	the **onset (lag or bolus arrival)** time of an enhancement curve i.e. the time from the CA injection to the appearance of contrast in the tissues.
ME	Maxt S(t)-**the maximum signal intensity (peak enhancement)** of a given time-varying signal S(t).
ME_a	ME-S_0-the **peak maximal absolute enhancement** of a given signal S(t), i.e., the difference between Sm and baseline (S_0) intensities.
$\frac{ME}{S_0}$	the **relative signal intensity (RSI)** or **peak enhancement ratio (PER)**, i.e., the relative peak enhancement.
TTP	the **time-to-peak**, i.e., the time before the CA reaches its highest value in the tissue during the first-pass cycle.
T_{90}	the time before the CA in the tissue reaches 90% of the maximal signal intensity
$\frac{ME}{TTP}$	the **maximum intensity time ratio (MITR)**, i.e., the ratio between the peak enhancement ME and the time-to-peak TTP
$\frac{ME}{(TTP-T_0)}$	the **wash-in slope (the maximal or initial upslope)**, i.e., the slope of the line connecting S_0 and S_m points.
$\frac{(S_{max}-S_{final})}{(T_{max}-TTP)}$	the **wash-out slope (down-slope)**, i.e., the slope of the line connecting S_m and the last point of the signal curve S_final.
$\frac{(S_E-S_0)}{(S_L-S_0)}$	the **signal enhancement ratio (SER)** is the ratio of early to late contrast enhancement; where SE and SL are the early and late contrast signal intensities measured at predefined times of TE and TL, respectively.

4.2.2.2 Parametric Approaches

Parametric or quantitative hemodynamic indices of DCE-MRI data can be derived with physiological basics as they are intimately related to the study of the pharmacokinetics of the contrast agent, particularly their contributions within and elimination from the blood [70]. These approaches, aim to estimate kinetic parameters by fitting the acquired data into models that explain the underlying physiology while making some assumptions. There are several models available, differing in the assumptions and simplifications made and the choice of a particular model for perfusion quantification depends on many factors, such as imaged area, tissue's properties, whether the image volume allows for AIF determination, temporal resolution, and many other.

The parametric kinetic models can be categorized in compartmental models or spatially distributed kinetic models based on whether they assume the existing tissues to be a finite number of interacting homogeneous compartments or assume the compartments to be infinitesimal. The principal assumption is that the human body can be represented by one or more "compartments" into and out of which the contrast agent dynamically flows. Another assumption is that in each compartment the CA is uniformly distributed throughout the volume.

Well-known compartmental models are based on the principles of the Kety's model [62]. Usually, a two-compartment model is used as it is more realistic. These models consider the intravascular extracellular volume fraction to be the central compartment (v_p), also referred as blood plasma, and the extravascular-extracellular volume fraction to be the peripheral compartment (v_e) as depicted in Figure 4.3.

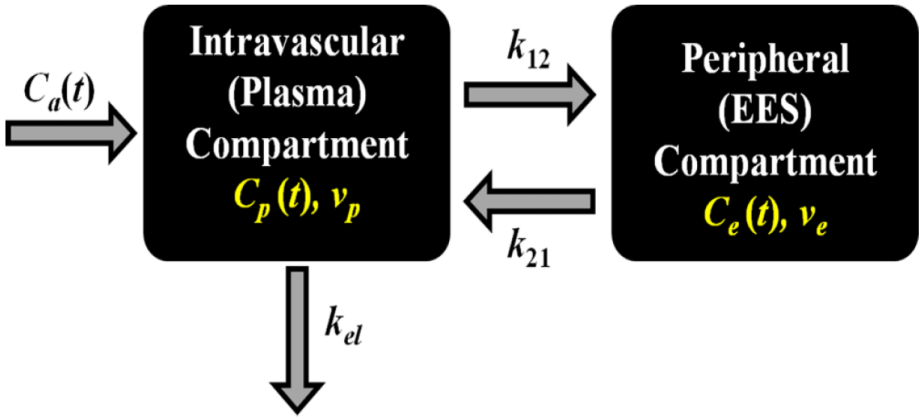

Figure 4.3: General representation of a two-compartment model used to describe the inherent physiology for perfusion parameter derivation. Adapted from [69].

In this model, the CA is introduced into the blood plasma by $C_a(t)$, yielding a dynamic concentration $C_p(t)$ in the first compartment. The CA will then diffuse into the extravascular-extracellular space (EES) in a reversible process characterized by a distribution rate constant (k_{12}) and a redistribution rate constant (k_{21}). The CA is eliminated in an irreversible process described by the rate constant k_{el}. Since, the parameters k_{12} and k_{21} control the CA transfer from the blood plasma to the tissue, they are related to capillary permeability. The total tissue concentration, $C_t(t)$, is described by:

$$C_t(t) = v_p C_p + v_e C_e(t) \tag{4.14}$$

, where v_p and v_e are the fractional plasma and EES volumes respectively, both with values between 0 and 1. One of the most common compartmental models and widely used in Brain Perfusion MRI quantification is the Tofts model and is described in detail below.

Tofts Model

The Tofts compartmental model was first proposed by [71] and unified many previous models while also introducing common characteristic parameters and naming conventions.

This model assumes that the contrast agent diffuses from and returns to the blood plasma at rates dependent on the forward transfer constant, k_{trans} (min^{-1}) and the reverse constant , k_{ep} (min^{-1}), as represented in Figure 4.4. It is considered a one-compartment model for weakly vascularized tissues as it ignores the intravascular compartment: $v_p = 0$. However nowadays, it is often applied in situations where the condition $v_p \approx 0$ is not necessarily fulfilled, for example in tumor scenarios, but where the data quality is inadequate to resolve any additional structure.

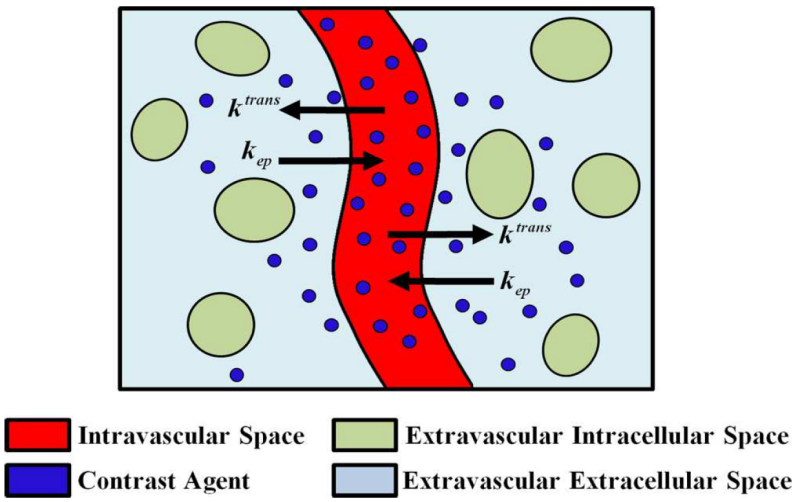

Figure 4.4: Schematic representation of the CA transfer in the Tofts model between the intravascular space and the EES space. Adapted from [69].

As the intravascular space volume contribution is ignored, the general equation to express the changes in the concentration of CA in the tissue is:

$$\frac{dC_t}{dt} = K_{trans}C_p(t) - k_{ep}C_t(t) = K_{trans}\left(C_p(t) - \frac{C_t(t)}{v_e}\right) \tag{4.15}$$

, where $k_{ep} = K_{trans}/v_e$. The CA concentration in the plasma, $C_p(t)$, after the injection specifies the AIF and is used as the initial condition to estimate $C_t(t)$. Therefore, at t=0, both concentrations are 0 and the previous Equation 4.15 can now be solved as:

$$C_t(t) = K_{trans}\int_0^t C_p(t')e^{-(K_{trans}/v_e)(t-t')}dt' \tag{4.16}$$

Physiologically, K_{trans} is the most important and significant tissue dependent parameter in the Tofts model. It assesses either plasma flow in flow-limited scenarios or tissue permeability in permeability-limited scenarios for the uptake. In mixed scenarios, it indicates a combination of the flow and permeability properties of the tissue and acts as a lump measure of their joint effect.

Chapter 5

Materials and Methods

The main focus of this work is to acquire both DSC and DCE data using SAGE EPIK, and quantify both data-sets to obtain perfusion parameters specific to each technique. In this chapter, the reader is presented with the materials and methods used throughout this study in order to complete the proposed goals. A brief description of the used data, equipment and acquisition protocol will be included, in addition to the image processing and data analysis description.

5.1 PET-MRI Scanner

All PET-MRI acquisitions of this project were performed at a bimodal scanner Siemens 3T hybrid MR/PET scanner at the FZJ INM-4 institute, allowing the simultaneous acquisition of MR and PET data. This hybrid scanner is a MAGNETOM TIM Trio System with an integrated Siemens BrainPET insert of high resolution, located inside of the MR bore and fixed with an air cushion 5.1.

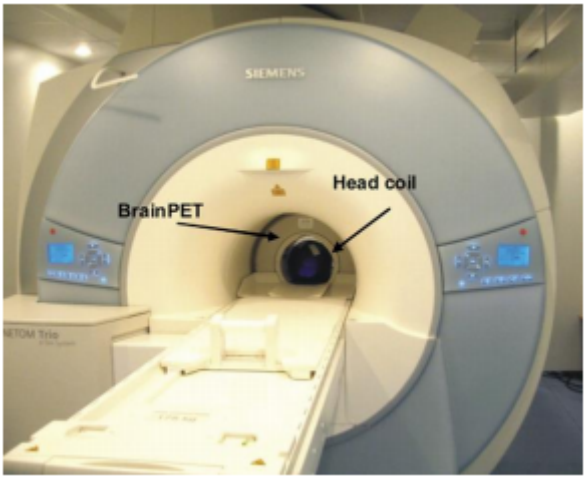

Figure 5.1: Forchungszentrum Juelich, INM-4 institute, 3TMR-BrainPET hybrid scanner for brain studies.

5.2 Datasets and Acquisition

5.2.1 Patients

Twenty-two patients with suspected brain tumor, recurrent tumor, or who required imaging of tumor stage progress were recruited for this study. Some patients were receiving or received radiotherapy, others had brain surgery for tumor removal, however this was considered not relevant for this study's outcome. Out of these twenty-two, fifteen patients (seven females and eight males) were fully diagnosed with a brain tumor and the resultant data sets were used in this study. Further information about the patients can be found in Appendix 7.1. If tumor histology was available, tumors were graded accordingly to the guidelines suggested by the *World Health Organization* (WHO) [55]. However, this information was generally not present, as it requires a biopsy. After a complete description of the study, written informed consent was obtained prior to scanning.

5.2.2 MRI acquisitions

An inversion recovery EPIK sequence, previous to contrast injection, for T_1-mapping was performed. For this sequence a repetition-time of 60 ms, a flip-angle of 25° and a echo-time of 25 ms were used for 63 time points. Thirteen slices with a matrix size of 96×96 were acquired.

Following contrast injection, perfusion weighted images were acquired using the combined 5-echo GESE EPIK sequence with a SPARSE factor of 3, described in the Section 2.4.5. A 90 degree pulse was applied, succeeded by two gradient echoes with the echo-times of 12 ms and 28 ms, respectively. Next, a refocusing pulse of 180 degrees followed by the two remaining gradient echoes and the spin-echo, with the echo-time of 54 ms, 70 ms and 85 ms, respectively. For this sequence, repetition-time was set to 1500 ms and 13 slices with a thickness of 3mm were acquired with a matrix size of 96×96, parallel imaging acceleration (R=2), partial Fourier= 5/8 and a field of view of 240 mm. For better understanding, a protocol scheme was included in Figure 5.2.

For each one of the twenty-two subjects, Gadoteric acid (Dotarem Guerbet) was injected with a dose of 0.1 mmol/Kg of body weight and 100 volumes were acquired in order to track dynamic signal changes induced by the contrast agent. Injection was performed automatically with a power injector (Injektron 82 MRT Medtron AG) at a flow rate of 5 ml/s.

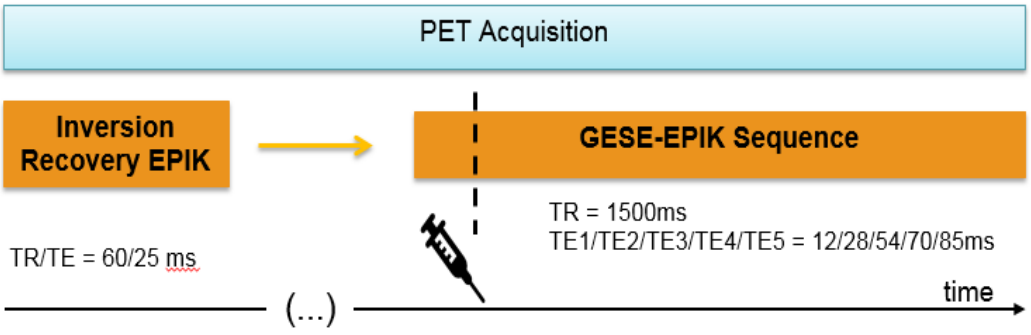

Figure 5.2: Scheme of imaging protocol.

5.2.3 PET acquisitions

Simultaneously with the MR measurements, a ^{18}F-FET PET scan was carried out in the hybrid scanner. For that, an intravenous injection of 3 MBq of ^{18}F-FET/kg was injected [72]. PET data were reconstructed using ordinary Poisson-OSEM 3D ([73]) algorithm with 4 subsets, 15 frames with 60 seconds each and 32 iterations. The reconstructed images have an isotropic voxel size of 1.25 mm^3 with a matrix size of 256×256×153. In addition, all images were post processed using a 3D Gaussian filter and motion corrected with the aid of "Pmod" software [74]. Note that, the BrainPET is a head only high-resolution PET insert with an isotropic centre resolution of 3 mm [75].

5.3 Post processing and analysis

The MRI data was analyzed using MATLAB v.2017 and v.2015a (The MathWorks, Inc, USA) [76] with the addition of the function *fitdcemri* [77] and in-house developed scripts. The PET data was visualized using the Amide's a Medical Image Data Examiner (AMIDE) [78].

The acquired and processed PET images were used for confirmation of existent tumor in the patient. If the images did not show an active area, the patient was removed from the set and further analysis was not performed.

5.3.1 DSC-MRI

5.3.1.1 Signal Conversion

The concentration-time curves in DSC-MRI are generated based on an assumed linear relationship between the contrast agent and the change in the apparent transverse relaxation rate by the first passage of the contrast agent through the vasculature:

$$\Delta R_2^*(t) = \frac{1}{T_2^*(t)} - \frac{1}{T_{2_0}^*} = k_2[Gd](t) \tag{5.1}$$

,where k_2 is a constant dependent on the transverse relaxivity, field strength, pulse sequence, vascular morphology and the contrast agent composition [79]. For the injected contrast, k_2 has a value of 4.9 L/mmol-s at 3 T [80].

The signal, S, measured over time, t, from DSC-MRI using a gradient echo-based sequence can be described by equation 4.4. By inverting this equation, an expression for $T_2{}^*(t)$ can be obtained:

$$\frac{1}{T_2^*(t)} = \frac{-1}{TE}\, ln\left[\frac{S(t)}{M_0 \sin\alpha \left[\frac{1-e^{\left(-\frac{TR}{T_1(t)}\right)}}{1-cos\alpha\, e^{\left(-\frac{TR}{T_1(t)}\right)}}\right]}\right] \tag{5.2}$$

Correspondingly, for $T_{2_0}{}^*$, a similar equation is obtained where S(t) no longer represents all the signal throughout the acquisition time, Equation 5.3. It represents only the data before the contrast detection in

the tissues of interest, in other words, the baseline signal S_B. Correspondingly, $T_1(t)$ is now T_{1_0}.

$$\frac{1}{T_{2_0}^*} = \frac{-1}{TE}\, ln \left[\frac{S_B}{M_0 \sin\alpha \left[\frac{1-e^{\left(-\frac{TR}{T_{1_0}(t)}\right)}}{1-cos\alpha\ e^{\left(-\frac{TR}{T_{1_0}(t)}\right)}} \right]} \right] \tag{5.3}$$

Adjusting equation 5.1 with equation 5.2 and 5.3:

$$\Delta R_2^*(t) = \frac{-1}{TE}\, ln \left[\frac{S(t)}{\left[\frac{1-e^{\left(-\frac{-TR}{T_1(t)}\right)}}{1-cos\alpha\ e^{\left(-\frac{-TR}{T_1(t)}\right)}} \right]} \frac{\left[\frac{1-e^{\left(-\frac{TR}{T_{1_0}(t)}\right)}}{1-cos\alpha\ e^{\left(-\frac{TR}{T_{1_0}(t)}\right)}} \right]}{S_B} \right] \tag{5.4}$$

The obtained equation 5.4 shows the potential effects of T_1 relaxation on the concentration curve. If the BBB remains intact, one can assume the contrast agent to remain within the blood vessels, no extravasation occurs and the T_1 is equal through time. This leads to the simplified equation 4.5.

For the first gradient echo (TE=12 ms), the concentration curve was calculated using equation 5.1, where $\Delta R_2{}^*$ results from equation 5.4.

However, since the tumors actually tend to disrupt the BBB, it is of high relevance to quantify the contrast agent concentration while taking into account the extravasation effects resultant from this disruption. Multi-echo acquisition methods are quite useful for this purpose, as the ratio between two signal curves of different echo times allows for the desired quantification without any over assumptions. From equation 4.4, the signal for the 1st and 2nd echo are:

$$S_{TE_1}(t) = M_0 sin(\alpha) \cdot \left[\frac{1-e^{\left(-\frac{TR}{T_1(t)}\right)}}{1-cos(\alpha)\cdot e^{\left(-\frac{TR}{T_1(t)}\right)}} \right] \cdot e^{\left(-\frac{TE_1}{T_{2*}(t)}\right)} \tag{5.5}$$

and

$$S_{TE_2}(t) = M_0 sin(\alpha) \left[\cdot \frac{1-e^{\left(-\frac{TR}{T_1(t)}\right)}}{1-cos(\alpha)\cdot e^{\left(-\frac{TR}{T_1(t)}\right)}} \right] \cdot e^{\left(-\frac{TE_2}{T_{2*}(t)}\right)} \tag{5.6}$$

The ratio between these two equations then becomes an expression of $T_2{}^*(t)$

$$\frac{1}{T_2^*(t)} = \frac{1}{TE_2 - TE_1} ln \left(\frac{S_{TE_1}(t)}{S_{TE_2}(t)} \right) \tag{5.7}$$

The pre-contrast apparent transverse relaxation, $T_{2_0}{}^*$, rate is similarly calculated. Again, adjusting equation 5.1, the following expression is obtained:

$$\Delta R_2^*(t) = \frac{1}{TE_2 - TE_1} ln\left(\frac{S_{TE_1}(t)}{S_{TE_2}(t)} \frac{S_{TE_{2B}}}{S_{TE_{1B}}}\right). \tag{5.8}$$

This expression was used to calculate the concentration curves with T_1 leakage correction.

In parallel, one could alternatively calculate the concentration curves using the spin-echo data where a linear relationship between the contrast agent and the change in transverse relaxation rate by the passage of the contrast agent through the vasculature can also be assumed:

$$\Delta R_2(t) = \frac{1}{T_2(t)} - \frac{1}{T_{2_0}} = k_2[Gd](t) \tag{5.9}$$

,where k_2 is a constant dependent on the transverse relaxivity, field strength, pulse sequence, vascular morphology and the contrast agent composition [79]. For the injected contrast, k_2 has a value of 4.9 L/mmol-s at 3 T [80]. For a spin-echo MRI sequence, with a flip angle of 90° the signal equation is:

$$S(t) = M_0 sin(\alpha) \cdot \left[1 - e^{\left(-\frac{TR}{T_1(t)}\right)}\right] \cdot e^{\left(-\frac{TE}{T_2(t)}\right)} \tag{5.10}$$

,where M_0 is proportional to the equilibrium magnetization and α is the flip angle used in imaging. In order to measure the changes that occur in T_2 , all acquired data are compared to a baseline signal at time t=0. Considering that the T_1 changes are small within tissue, equation 4.4 can be simplified to

$$\Delta R_2(t) = \frac{-1}{TE_5} ln\left(\frac{S_B}{S_{SE}(t)}\right) \tag{5.11}$$

Based on a multi-echo DSC sequence and considering that the contrast changes are slower than the time scale of T_1, the spin-lattice changes can also be obtained [81].

To obtain a T_1 weighted signal, the signals from the first two echoes can be combined by extrapolating the data to zero echo time (TE=0)

$$S_0 = S_1 \, e^{\frac{TE_1}{TE_2 - TE_1} \, ln\left(\frac{S_1}{S_2}\right)} \tag{5.12}$$

, where S_0 will correspond to a set of images with the same parameters as the resultant from the MRI sequence, but influenced by T_1 changes only. This way, T_1 leakage correction can be performed also for T_2-weighted data from the spin-echo, as follows:

$$\Delta R_2(t) = \frac{-1}{TE_5}\left[ln\left(\frac{S_{B_{TE_5}}}{S_{TE_5}(t)}\right) - ln\left(\frac{S_{B_{TE_0}}}{S_{TE_0}(t)}\right)\right] \tag{5.13}$$

Due to the fact that the previously described method only makes use of two of the five echoes in the GESE-EPIK sequence, another approach to calculate the R_2 and $R_2{}^*$ was applied. This approach aims to better estimate the R_2 and $R_2{}^*$ by using a nonlinear least squares fitting to a piecewise function (equation

5.14) as described in [82]:

$$S(\tau) = \begin{cases} S_0^I \, e^{-\tau R_2^*} & , 0 < \tau < TE_5/2 \\ S_0^{II} \, e^{-TE*(R_2^* - R_2)} \, e^{-\tau(2\times R_2 - R_2^*)} & , TE_5/2 < \tau < TE_5 \end{cases} \tag{5.14}$$

,where $S_0{}^I$ and $S_0{}^{II}$ correspond to the baseline signal. Since a nonlinear fitting takes a lot of computational memory and time, the equation was transformed into a linear relationship instead. For each point in time, the signal from the four echoes is combined into the following matrix system:

$$\begin{bmatrix} lnS_{TE_1} \\ lnS_{TE_2} \\ lnS_{TE_3} \\ lnS_{TE_4} \end{bmatrix} = \begin{bmatrix} -TE_1 & 0 & 1 & 0 \\ -TE_2 & 0 & 1 & 0 \\ TE_3 + \tau & -2TE_3 + \tau & 0 & 1 \\ TE_4 + \tau & -2TE_4 + \tau & 0 & 1 \end{bmatrix} \times \begin{bmatrix} R_2^* \\ R_2 \\ lnS_0^I \\ lnS_0^{II} \end{bmatrix} \tag{5.15}$$

, which can be represented as Y=A $\times$ X . The values for R_2 and $R_2{}^*$ are calculated by X= A^{-1} $\times$ Y. This method tries to better estimate the concentration curve, considering T_2 and $T_2{}^*$ effects.

5.3.1.2 Brain Mask

In order to remove unwanted signal data from outside the brain region, a set of brain masks were computed, one mask for each available slice.

As a starting point, a global threshold was found, following Otsu's method [83] and all values above the threshold were set to one, under the threshold were set to zero. For every slice, from all five echo data, a binary mask is created. All the five brain masks from the same slice are, then, combined to originate only a mask per slice. This method for mask creation was choosen due to its simplicity.

Since the masks are binary, they are easily multiplied to each available data image, reducing them to the area of interest - the brain.

5.3.1.3 AIF estimation

For the quantification of DSC-MRI parameters, an accurate arterial input function that represents the concentration of the contrast agent in the blood plasma is of high relevance. Therefore, special attention must be paid when choosing the method to obtain the AIF [84].

In order to avoid the need of a highly trained staff, reduce subjective errors and decrease the time for AIF estimation, an automatic method was used.

The chosen method starts by identifying the time-point correspondent to the lowest signal intensity, *tmin*, which corresponds to the highest amount of contrast agent in the blood's plasma. Then, a search for the image's voxels where the bolus' peak occurred before the time-point *tmin* was performed. The concentration curves for all the voxels that matched the criteria were obtained and organized by order of peak intensity, from lowest to highest. The highest five were averaged resulting in a global AIF. A global

AIF is a term used to refer to one only AIF that is used for all of the existent pixels.

This method was repeated for the concentration curves obtained from the previous section, in order to compare the T_1 leakage correction with the uncorrected version.

5.3.1.4 Parameter Quantification

After defining the required AIF, calculating the concentration curves and obtaining a proper brain mask, DSC-MRI parameters ought to be calculated.

For each available patient, all parameters were calculated in the three previously described ways with the only difference being the correction performed on the calculus of the concentration curves and the correspondent AIF. The cerebral blood volume was computed from equation 4.11 as the ratio between the area under the curve (AUC) from the concentration curve through time and the AUC of the AIF through time. Cerebral blood flow was calculated using the maximum of the impulse response function, represented in equation 4.10 from the circular singular value decomposition (SVD). Additionally, the mean transit time was computed as the ratio between CBV and CBF, as stipulated in equation 4.12.

5.3.2 DCE-MRI

5.3.2.1 Signal Extrapolation

From Section 5.3.1.1, equation 5.12 allowed the estimation of a set of T_1-weighted images used to correct the leakage effects from BBB disruption of the T_2-weighted time curves. Another use of this extrapolated data would be quantification of DCE-MRI, as this technique requires nothing else but, T_1-weighted images acquired through contrast injection [81].

5.3.2.2 Signal Conversion

Conventional DCE-MRI concentration curves are generated based on a assumed linear relationship between the contrast agent and the change in spin-lattice relaxation rate, represented by equation 5.16.

$$\Delta R_1^*(t) = \frac{1}{T_1^*(t)} - \frac{1}{T_{1_0}^*} = k_1[Gd](t) \tag{5.16}$$

,where k_1 is a constant dependent on the transverse relaxivity, field strength, pulse sequence, vascular morphology and the contrast agent composition [79]. For the injected contrast, k_1 has a value of 3.5 L/mmol-s at 3 T [80].

The signal, S, measured over time, t, from DCE-MRI using a gradient echo-based sequence can be described by equation 4.4. By inverting this equation, an expression for T_1(t) can be obtained:

$$\frac{1}{T_1(t)} = \frac{-1}{TR}\, ln\left[\frac{M_0 \sin\alpha\, e^{\left(-\frac{TE}{T_2(t)}\right)} - S(t)}{M_0 \sin\alpha e^{\left(-\frac{TE}{T_2(t)}\right)} - S(t)cos\alpha}\right] \tag{5.17}$$

Following the same methodology described for DSC-MRI, an expression for $1/T_{1_0}$ can be obtained, quantifying the spin-lattice relaxation rate previous to contrast injection.

$$\frac{1}{T_{10}} = \frac{-1}{TR}\, ln \left[\frac{M_0 \sin\alpha\, e^{\left(-\frac{TE}{T_{2_0}}\right)} - S_B}{M_0 \sin\alpha e^{\left(-\frac{TE}{T_{2_0}}\right)} - S_B cos\alpha} \right] \tag{5.18}$$

Combining equation 5.16 with equations 5.17 and 5.18:

$$\Delta R_1(t) = \frac{-1}{TR}\, ln \left[\left[\frac{M_0 \sin\alpha\, e^{\left(-\frac{TE}{T_{2(t)}}\right)} - S(t)}{M_0 \sin\alpha e^{\left(-\frac{TE}{T_{2(t)}}\right)} - S(t) cos\alpha} \right] \left[\frac{M_0 \sin\alpha\, e^{\left(-\frac{TE}{T_{2_0}}\right)} - S_B}{M_0 \sin\alpha e^{\left(-\frac{TE}{T_{2_0}}\right)} - S_B cos\alpha} \right] \right] \tag{5.19}$$

This equation 5.19 demonstrates the potential influence of T_2^* effects on the concentration curves obtained with DCE-MRI. From equation 4.4, assuming fully relaxed spins, M_0 can be estimated from a single-shot, single repetition, in a limit that TR $\rightarrow \infty$. Equations 5.5 and 5.6 become:

$$S_{TE_{1_0}} = M_0 sin(\alpha) \cdot e^{\left(-\frac{TE_1}{T_{2_0}}\right)} \tag{5.20}$$

and

$$S_{TE_{2_0}} = M_0 sin(\alpha) \cdot e^{\left(-\frac{TE_2}{T_{2_0}}\right)} \tag{5.21}$$

Again, the ratio between these two equations then becomes an expression of T_2^*(t). Replacing this ratio into equation 5.20 allows for the estimation of M_0:

$$M_0 = \frac{S_{TE_{1_0}}}{sin\alpha} e^{\frac{TE_1}{TE_2 - TE_1} ln\left(\frac{S_{TE_{1_0}}}{S_{TE_{2_0}}}\right)} \tag{5.22}$$

,where $S_{TE_{1_0}}$ and $S_{TE_{2_0}}$ are , respectively, the first image from the first and second gradient echoes. For equation 5.19, S(t) becomes the extrapolated data calculated from expression 5.12.

Since the data applied to calculate ΔR_1 results from an extrapolation to TE=0, one can assume that, over time, occurs insignificant phase dispersion. This means that T_2^* effects can be ignored, which results in:

$$\Delta R_1(t) = \frac{-1}{TR}\, ln \left[\left[\frac{M_0 sin\alpha - S(t)}{M_0 sin\alpha - S(t) cos\alpha} \right] \left[\frac{M_0 sin\alpha - S_B}{M_s in\alpha - S_B cos\alpha} \right] \right] \tag{5.23}$$

Two different concentration curves were calculated from equation 5.23: one where S_B corresponds to the data acquired from the T_1-mapping previous to contrast, and another where S_B results from averaging the first eight time-points of the extrapolated image (baseline signal).

5.3.2.3 Brain Mask

For DCE-MRI analyses, the brain mask obtained from the DSC-MRI data was applied to all DCE-MRI extrapolated images and data.

5.3.2.4 AIF estimation

For DCE-MRI analyses, the AIF calculated from the DSC-MRI data and corrected for T1 leakage effects was used for all parameter quantification analyses.

5.3.2.5 Parameter Quantification

To fully quantify perfusion DCE-MRI parameters, a kinetic model, that represents the physiology of the inherent tissues and allows for the accurate estimation of perfusion parameters, must be applied to the data.

Due to its simplicity and general use in brain tumor studies, the Tofts model was selected among the many kinetic models available. The Tofts model was applied by means of the, already referred, matlab function *fitdcemri*. This function required the input of the concentration curve for all pixels, the AIF and a time vector. As outputs, the function computed the parameters K_{trans} and k_{ep} and the value R^2 which indicates the degree of proximity of the applied model fitting to the measured real values. The model was applied 3 times for a differente set of inputs:

1. Concentration curve calculated with usage of T_1-mapping previous to contrast and uncorrected AIF for T_1 leakage;
2. Concentration curve calculated with usage of T_1-mapping previous to contrast and corrected AIF for T_1 leakage;
3. Concentration curve calculated with usage of only extrapolated data and corrected AIF for T_1 leakage;

All models were set to have a R^2 higher than 90% to increase the accuracy of the fitted model.

5.3.3 Brain Tumor Analysis

Several DSC- DCE-MRI studies have tried to link the tumor histology or the tumor response to treatment, with the obtained perfusion parameters. Although not a main objective of this study, if the data were to be available, investigation on this matter ought to be done.

However, histology reports for all patients were not available, as it involves the invasive acquisition of a tumor biopsy. Since the tumor type was not known, tumor grading was not possible and, therefore, further analysis of this matter was not pursued.

Chapter 6

Results and Discussion

In the following chapter, the obtained results from all performed tests from Chapter 5 and respective analysis are here presented.

6.1 PET

From the applied imaging protocol, several image data-sets were acquired. As already referred, the PET images were only used as a filter of patients relevant for the perfusion quantification study. For example, in Figure 6.1, the patient does not present an activated region with the radio-pharmaceutical tracer, leading to the deduction that there is no tumor. This patient was not further included in the present work. Meanwhile, Figure 6.2 depicts an activated region, confirming the existence of the tumor. This patient data was then fully analyzed and perfusion parameters were derived. From 22 patients, only 15 were selected for this study.

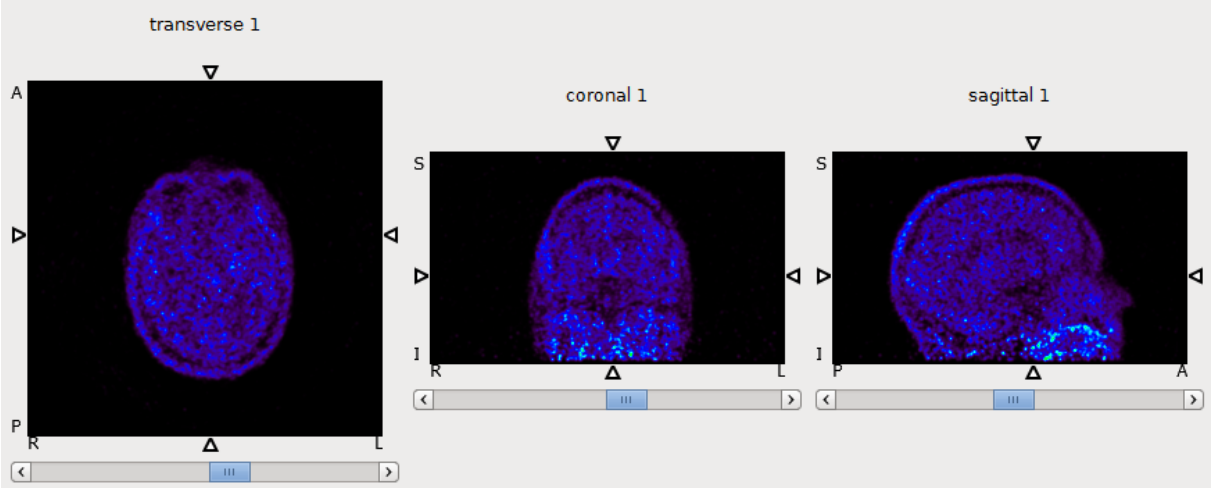

Figure 6.1: ^{18}FET-PET images for a negative tumor patient. No active region is shown.

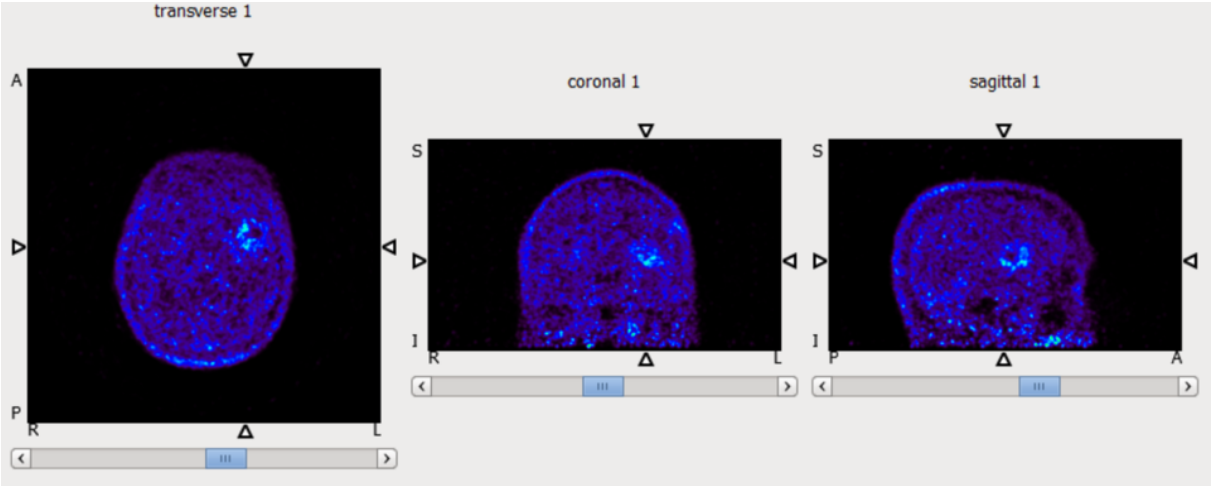

Figure 6.2: ^{18}FET-PET images for an identified tumor patient. The tumor is easily identified on the right hemisphere of the brain.

6.2 DSC-MRI

Resultant from the Multi-Echo GESE-EPIK sequence protocol, 13 slices for 100 time points for 5 echoes were acquired, i.e. in total, 500 images. In Figure 6.3, an example of the acquired images, for a random patient, are shown.

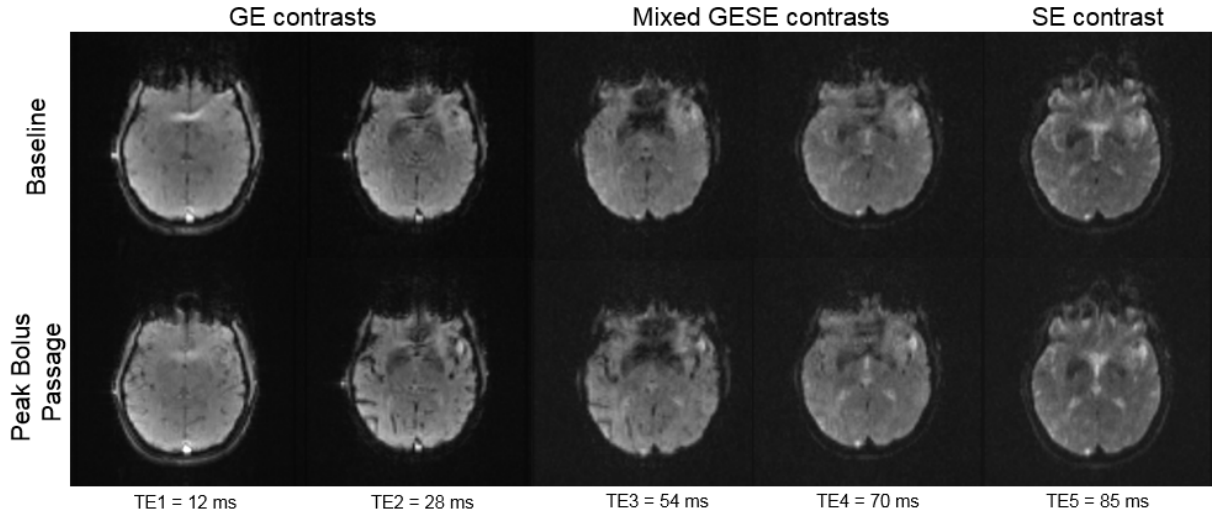

Figure 6.3: GESE EPIK images with GE, GESE and SE contrast. The top row shows the five echoes at the baseline while the bottom row shows the images at the peak bolus passage.

The top row includes a slice for each of the acquired echoes for a baseline point, while the bottom row shows the same slice for the peak bolus passage. A small area on the right hemisphere, in the anterior plane, is enhanced with the contrast agent passage, identifying the tumor region.

Figure 6.4 shows the time curve of the signal intensity depicting the arrival of the contrast agent in a single, representative gray matter voxel. Despite the unclarity of presented image due to multi-echoes display with different intensities each, for all echo times it was possible to clearly track the dynamic

signal changes even though a higher signal drop was found in the earlier echoes compared to the later ones.

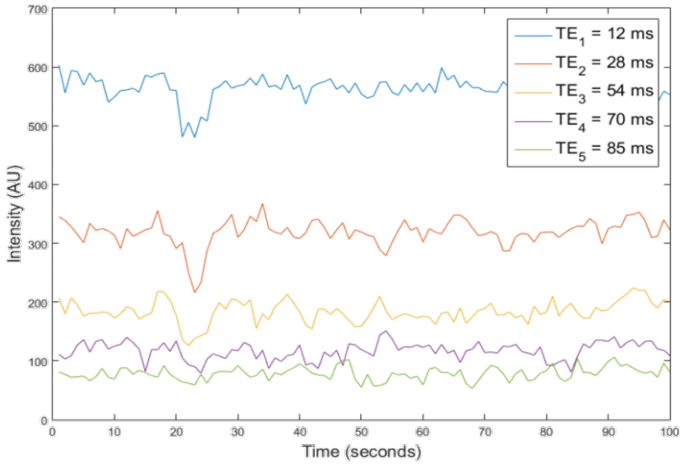

Figure 6.4: Signal intensity time course for the different echoes showing the arrival of the contrast agent.

6.2.1 Signal Conversion

In Section 5.3.1.1, the processes of how acquired data was used to calculate the required concentration curves were described. From equations 4.5, 5.8 and 5.15, $\Delta R_2{}^*$ curves were calculated and plotted in Figure 6.5 (left). To clarify, the curve referred to as *matrix* corresponds to the result from equation 5.15 ; equation 5.8 to the curve $\Delta R_2{}^*$ *with leakage correction*; and the *uncorrected* curve to equation 4.5 derived data.

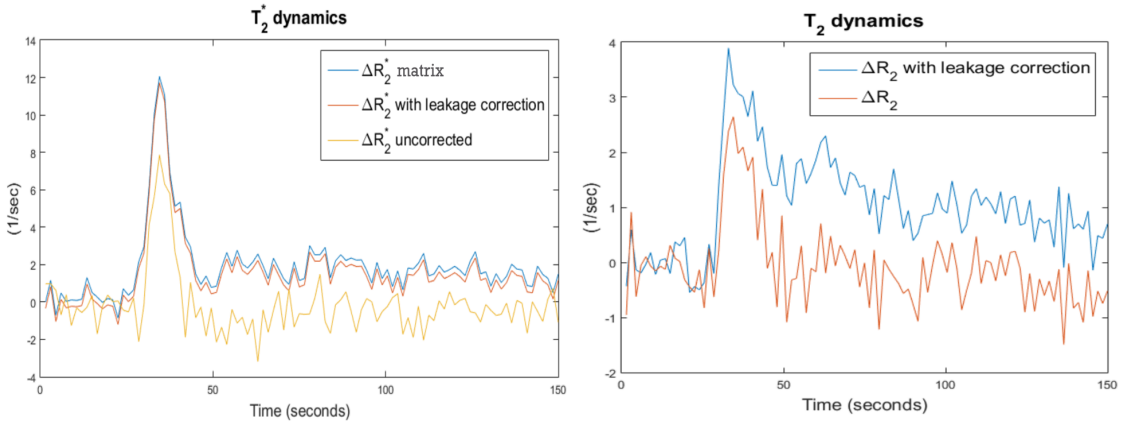

Figure 6.5: $T_2{}^*$-weighted time course data derived from 5 echoes-matrix; with and without T_1 correction are depicted (left). T_2-weighted time course data with and without T_1 correction are depicted (right).

T_1 leakage effects generally cause an underestimation of the peak bolus and negative values following the peak curve where one would expect some contrast re-circulation. By analyzing the plotted curves, it is observed that the uncorrected $\Delta R_2{}^*$ curve portraits exactly the mentioned leakage effects. Meanwhile,

the other two curves, accurately demonstrate the applied correction, showcasing the benefits of multi-echo sequences.

However, if one were to compare the two successful methods, the matrix methods involves more computational power and time which do not justify its further usage in this study where only patients with well-identifiable tumors are included. Perhaps patients where a higher precision is required, would benefit from this last method.

From equations 5.11, 5.13 ΔR_2 curves were calculated and plotted in Figure 6.5 (right). Similarly to the ΔR_2^*, the T_1 leakage effects were successfully corrected through the usage of equation 5.13. In opposition to the uncorrected curve, the corrected apparent transverse relaxation rate does not present negative values, nor was underestimated. Both relaxation rates were rectified, avoiding possible errors in the parameter quantification, resultant from this component.

6.2.2 Brain Mask

As described in Section 5.3.1.2, a brain mask for each slice was created to remove all signal from outside of the brain area. An example of the resultant slice can be seen in Figure 6.6. Although some random pixels from outside the skull were still included, the majority of the unwanted voxels were successfully unaccounted for.

Brain masks are particularly useful in perfusion MRI quantification as they allow the selection of the areas of interest for the quantification, removing unnecessary computational time on uninteresting areas.

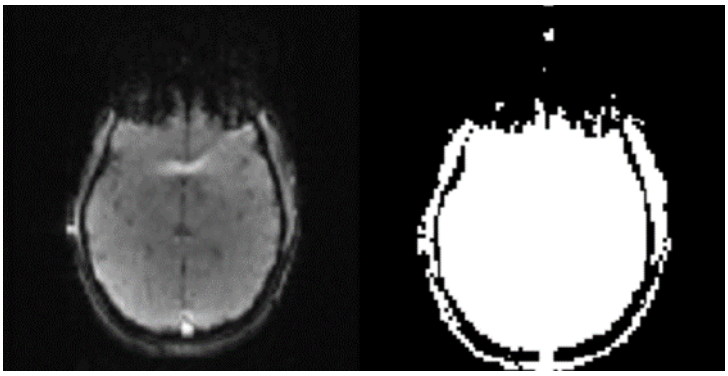

Figure 6.6: On the left, an image from the first echo. On the right, the respective slice applied mask.

6.2.3 AIF estimation

The arterial input function is a requirement for perfusion quantification in order to accurately determine the time rate of change of the contrast agent's concentration in blood plasma. The accuracy of the AIF significantly influences the precision of the pharmacokinetic parameters extracted. Therefore, the incorrect estimation of this function has severe consequences in both DSC and DCE-MRI quantification. If the arterial blood flow is not fully saturated or the T_1 leakage effects are uncounted for, this leads to an overestimation of the AIF [85]. MRI signal amplification or blood flow pulsatility are also factors that lead to incorrect estimation of the AIF [86], [87].

In this work, T_1 leakage effects are one of the biggest source of errors. For this reason, it is of high priority to correct the extravasion of CA leading to incorrect estimation of the AIF. In Figure 6.7 it is shown both the uncorrected and the corrected version of the AIF. It can be observed that the peak intensity of the uncorrected curve is more than twice higher than the corrected version. It is concluded that the correction performed for the AIF was successful, addressing the issue of overestimation.This overestimation would have led to wrongly quantified parameters, inducing misinterpretation of the patient condition. This is a strong example of the importance of accounting for T_1 effects and overestimation of the AIF.
The influence of the AIF is further studied in the next sections in addition to the effects of CA extravasion.

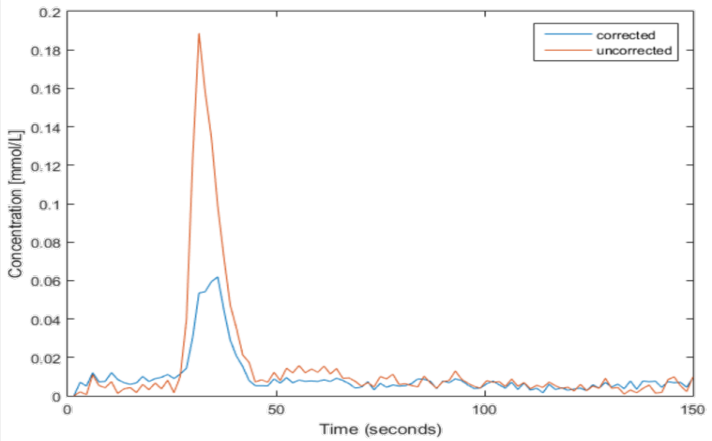

Figure 6.7: Derived AIF from T_2^* uncorrected and corrected for T_1 leakage effects.

6.2.4 Parameter Quantification

In order to address the real effects of the performed corrections for T_1 leakage effects and AIF overestimation, parameters of perfusion DSC-MRI were calculated for both uncorrected and corrected apparent transverse relaxation rates.

Throughout this section, for a patient, images presenting each quantitative parameter are shown. In the presented figures, image 1) results from calculating the respective parameter map while using uncorrected data, while image 2) results from corrected data usage. By data, it refers to both the ΔR_2^* curve and the AIF. In addition, a table including values for the tumor, white and gray matter tissues, from the same patient, were also included for each of the parameters for a more direct comparison.

All the acquired values and parameters maps were compared with the available literature ([88], [89],[90]). For healthy tissue, CBF usually has values between 10-100 mL/s/100gr; CBV between 0.1-8 mL/100gr; and MTT between 0.01-0.3s. For tumor tissue, CBF usually has values between 50-300 mL/s/100gr; CBV between 2-30 mL/100gr; and MTT between 0.01-0.4s. This comparison with only the literature had to be performed because another DSC-MRI sequence could not be acquired. Several impediments lead to the impossibility of another perfusion sequence acquisition. Firstly, each DSC-MRI perfusion sequence requires the injection of a contrast agent. If two sequences are acquired then, two bolus injections would have to be injected into the patient. This adds up to the amount of exogenous contrast that the kidneys will have to filter. If the patient has a healthy renal system this is already unadvised, moreover if the patient is elderly and has renal pathologies. Secondly, some studies have warned for the possibility of

Gadolinium accumulation in the brain tissue or/and bones [91]. More injections, mean further contrast agent accumulation. Lastly, it requires more acquisition time. Most of the patients in this study were debilitated and asking for twice the required extra time was not acceptable.

For these main reasons, the results were compared to the literature, as other have done before ([88], [89],[90]).

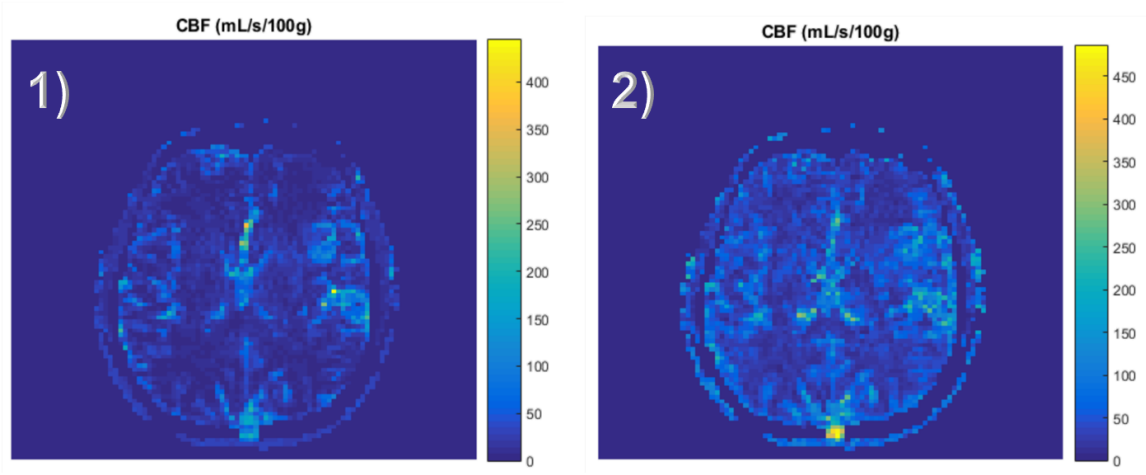

Figure 6.8: Cerebral Blood Flow for: 1) uncorrected; 2) corrected for T_1 leakage effects.

Table 6.1: CBF values for tumor, gray matter and white matter while using ΔR_2^* corrected and uncorrected of T_1 leakage effects.

	Tumor tissue	**Gray matter**	**White matter**
Uncorrected CBF [mL/s/100g]	153.5	40.31	8.07
Corrected CBF [mL/s/100g]	161.3	77.63	27.97

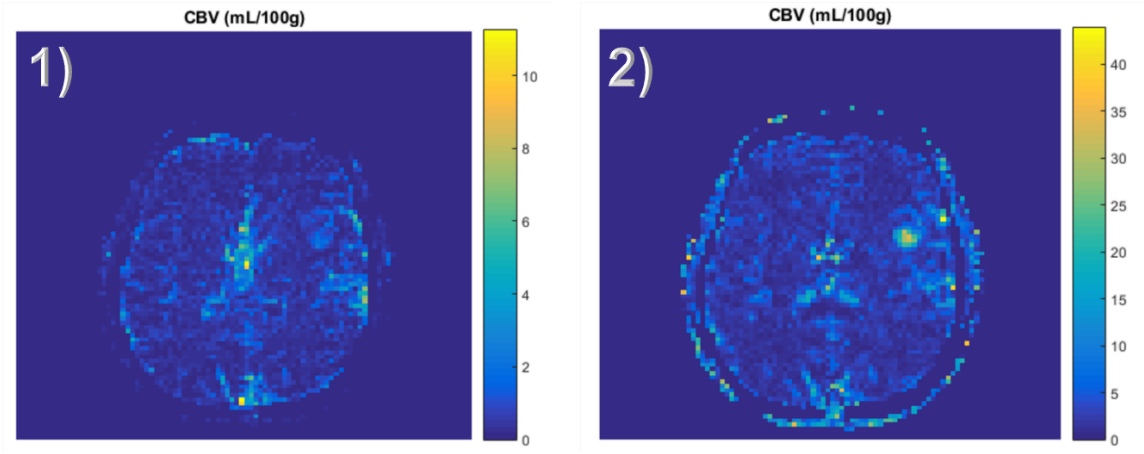

Figure 6.9: Cerebral Blood Volume for: 1) uncorrected; 2) corrected for T_1 leakage effects.

Table 6.2: CBV values for tumor, gray and white matter while using ΔR_2^* corrected and uncorrected of T_1 leakage effects.

	Tumor tissue	Gray matter	White matter
Uncorrected CBV [mL/100g]	2.0245	0.9626	0.39
Corrected CBV [mL/100g]	20.96	4.737	1.405

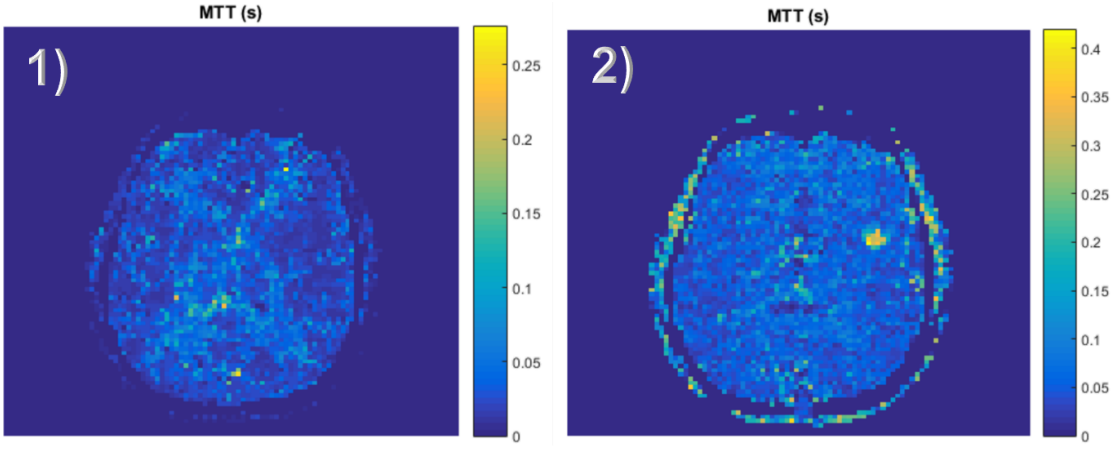

Figure 6.10: Mean Transit Time for: 1) uncorrected; 2) corrected for T_1 leakage effects.

Table 6.3: MTT values for tumor, gray matter and white matter while using ΔR_2^* corrected and uncorrected of T_1 leakage effects.

	Tumor tissue	Gray matter	White matter
Uncorrected MTT [s]	0.0132	0.0239	0.0483
Corrected MTT [s]	0.1299	0.0610	0.0502

For all three parameters, the influence of T_1 effects is clear by observing Figures 6.8, 6.9 and 6.10. The tumor, by disrupting the BBB, increases the amount of CA leaking into the EES of the tumor tissue, which unaccounted for, leads to the underestimation of the perfusion parameters. By comparing images 1) with 2) of all parameters, one can see a better delimitation of the tumor area in 2) where corrections were applied.

In addition, not only the tumor area was affected by the extravasion of the contrast agent, but also the gray and white matter tissues. By observing the values in Tables 6.1, 6.2 and 6.3, it is concluded that both tissues' perfusion DSC-MRI parameters were underestimated. This is potentially misleading as one can assume a tumor to be of a lesser severity when evaluating the values from the wrongly calculated curve without T_1 leakage correction. For all patients similar results were obtained and can be accessed in the created bar graphic for each of the parameters, Figure 6.11 (left), 6.12 (left) and 6.13 (left). An improvement can be generally seen in CBV, CBF and MTT.

Summing up, all obtained perfusion parameters were in accordance with the available literature and performed as expected, highlighting the tumor area from the healthy tissue. In addition, the performed corrections were effective and their importance was confirmed.

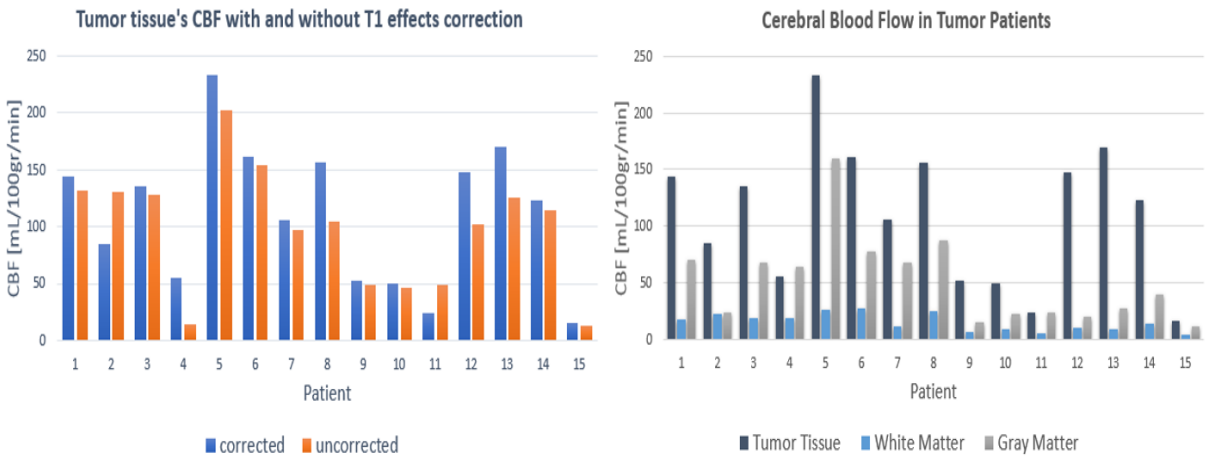

Figure 6.11: For all patients, the graphic presents: CBF values for tumor tissues calculated using corrected and uncorrected data of T_1 leakage effects (left); CBF values for three tissues, calculated using corrected data (right).

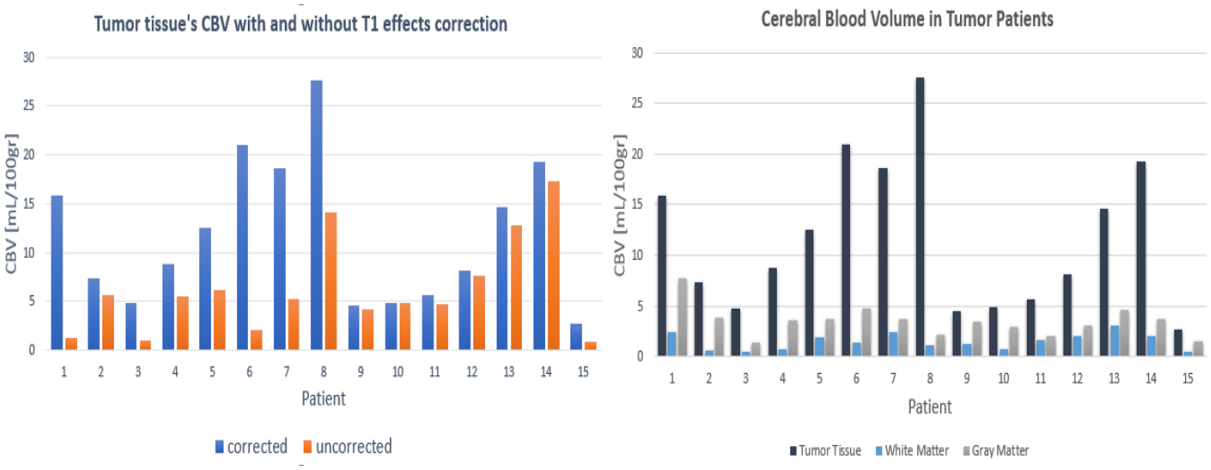

Figure 6.12: For all patients, the graphic presents: CBV values for tumor tissues calculated using corrected and uncorrected data of T_1 leakage effects (left); CBV values for three tissues, calculated using corrected data (right).

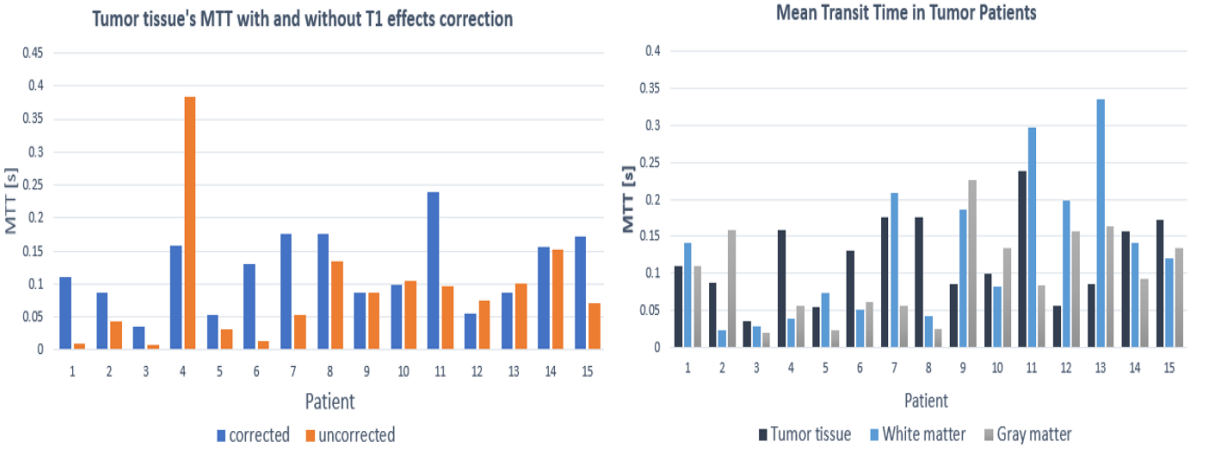

Figure 6.13: For all patients, the graphic presents: MTT values for tumor tissues calculated using corrected and uncorrected data of T_1 leakage effects (left); MTT values for three tissues, calculated using corrected data (right).

For each of the parameters, another bar graphic was made, containing, for each patient, values of three different tissues of interest: tumor, white matter and gray matter tissue. Analyzing the graphics on the right from Figures 6.11, 6.12 and 6.13 several conclusions can be reached.

Firstly, the bar graphics provided a visual evidence that the tumor tissue always has a higher signal than healthy tissues. This is resultant from tumor angiogenesis which increases the blood vessels surrounding the tumor area and, therefore, increases blood flow and blood volume to the area in question, augmenting the DSC parameters' values.
Secondly, the white matter values are always the lowest and around the same values. This serves as strong evidence that the parameters were not randomly calculated, but actually have some ground truth and correlate well with human physiology.
Thirdly, although at first look the same cannot be said about the gray matter tissue values, one must consider that the values were not measured from the same brain slice for all patients, as the tumors were localized in different regions. This slice variation causes differences in the calculation of the gray matter values, as some regions have more vascularization and a more intense presence of gray matter sulcus than others, for example the insular cortex.

However, there is still room for improvement, as some errors are still frequent in the analysis of the data and may have influenced the results. For example, the manual identification and selection of tissue areas for parameter estimation, might have induced errors by wrongly including voxels of another tissue through misidentifying the tissue type. Also, the MTT values for tumor tissue did not show any directly correlation with tumor tissue, having sometimes higher values for tumor tissue than for healthy but also vice versa.

In essence, full DSC-MRI perfusion quantification for all tumor patients was successfully achieved, properly delineating the unhealthy region of the brain. Once again, the usefulness of perfusion DSC-MRI was confirmed.

6.3 DCE-MRI

6.3.1 Signal Extrapolation

From equation 5.12, an extrapolated signal was calculated accounting only to T_1 changes. In addition to being used for leakage correction, the extrapolated signal was used for DCE-MRI quantification. However, confirmation that the signal was correctly extrapolated and indeed provided T_1-weighted information was required. Therefore, a slice from the baseline period and a slice after contrast agent detection were visualized. In addition, the difference between the two time sets was also calculated and visualized. As seen in Figure 6.14 (left), the difference between timepoints picture depicts signal enhancement in the tumor area meanwhile other regions remain dark ($\Delta = 0$). This confirms that the extrapolated signal registers changes throughout time, validating the usage of this data for DCE quantification.

For further confirmation, the signal versus time graphic was plotted for a selected region of interest in the tumor area and for a healthy area. In Figure 6.14 (right), the signal differences between tumor and healthy tissue can be identified. As expected, the tumor tissue has a sudden and high signal increase resultant from passage of the contrast agent from the blood vessels into the EES of the tumor tissue.

Meanwhile, healthy tissue, as there is no BBB disruption in these tissues, does not intake much of the contrast agent, therefore, its signal remains "constant" throughout time. This behavior was expected, as in accordance with the literature [54].

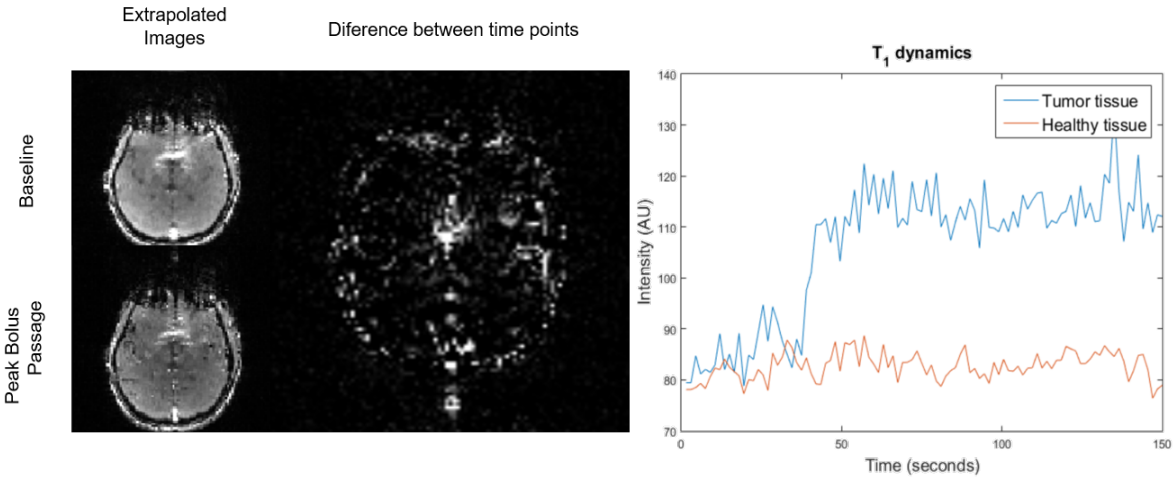

Figure 6.14: On the left, images from the extrapolated data for the a baseline timepoint, peak bolus passage timepoint and the diference between the two timepoints are shown. On the right, T_1-weighted time course from extrapolated data for tumor tissue and healthy tissue.

6.3.2 Signal Conversion

From equation 5.19, ΔR_1 curves were calculated and plotted in Figure 6.15 for tumor tissue. To clarify, the curve referred to as ΔR_1 *with* T_1 *mapping* corresponds to the result from replacing S_B with the data acquired from the T_1-mapping previous to contrast injection in equation 5.19; while ΔR_1 *without* T_1 *mapping* corresponds to the result from replacing S_B with the average baseline signal of the extrapolated signal itself.

Both curves have the expected behavior and reasonable values. In addition, the curves are similar sharing the same time of increase and similar maximum value. This is a strong indicator that both methods for calculating the longitudinal relaxation rate worked effectively.

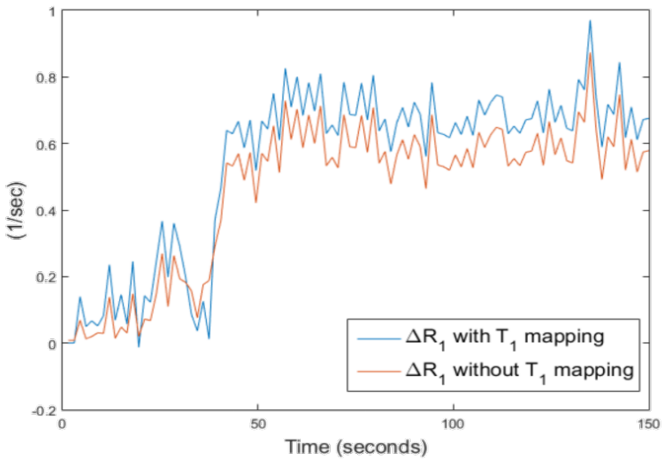

Figure 6.15: ΔR_1 time curves with and without the usage of the T_1-mapping acquired previous to contrast injection.

6.3.3 Parameter Quantification

To quantify DCE-MRI perfusion parameters, a kinetic model was applied to the extrapolated data. The Tofts model allows estimation of two perfusion parameters: K_{trans} and K_{ep}. K_{trans} refers to the flow of contrast agent into the tissue of interest, from the blood. K_{ep} refers to the flow of contrast agent leaving the tissue of interest into the vascular system. The blood flow is generally ignored in the Tofts model. All the acquired values and parameters maps were compared with the available literature [54], [92] and [93] for the same reason listed previously in Section 6.2.4. For healthy tissue, K_{trans} usually has values between 0.01-0.1 1/s and K_{ep} between 0.01-0.05 1/s. For tumor tissue, K_{trans} usually has values between 0.05-0.3 1/s and K_{ep} between 0.05-0.4 1/s.

Similarly to Section 6.2.4, in order to address the real effects of the performed corrections, perfusion parameters of DCE-MRI were firstly calculated using a longitudinal relaxation rate that made use of the acquired T_1-mapping at the beginning of the acquisition protocol with a) AIF without leakage effects correction; and b) AIF with corrections.
In addition, a table including values for the tumor, white matter and gray matter tissues, from the same patient, were also included for each of the parameters, to provide a more direct comparison between the tissues actual values.

The importance of the leakage effects correction and precise AIF estimation are, again, emphasized with the shown results in Figure 6.16 and 6.17, and Tables 6.4 and 6.5. A wrongly estimated AIF, leads to parameter underestimation. Although in DCE-MRI leakage effects are not a direct source of error, since the AIF was estimated from ΔR_2^* curves which need to account for this error source, indirectly contrast agent extravasion becomes a possible source of error. In Figure 6.18, both graphics exhibit the described effects for both parameters in all patients.

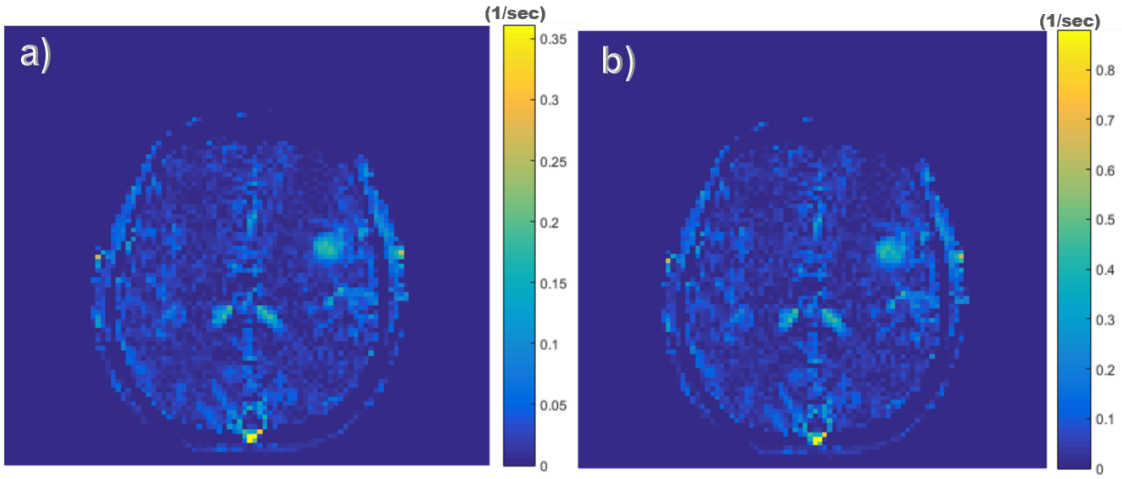

Figure 6.16: Ktrans resultant from model using a) uncorrected AIF b) corrected AIF for T_1 leakage effects.

Table 6.4: Ktrans values for tumor, gray matter and white matter while using AIF corrected and uncorrected of T_1 leakage effects.

	Tumor tissue	**Gray matter**	**White matter**
Uncorrected Ktrans [1/s]	0.1719	0.0479	0.0246
Corrected Ktrans [1/s]	0.3327	0.0433	0.0231

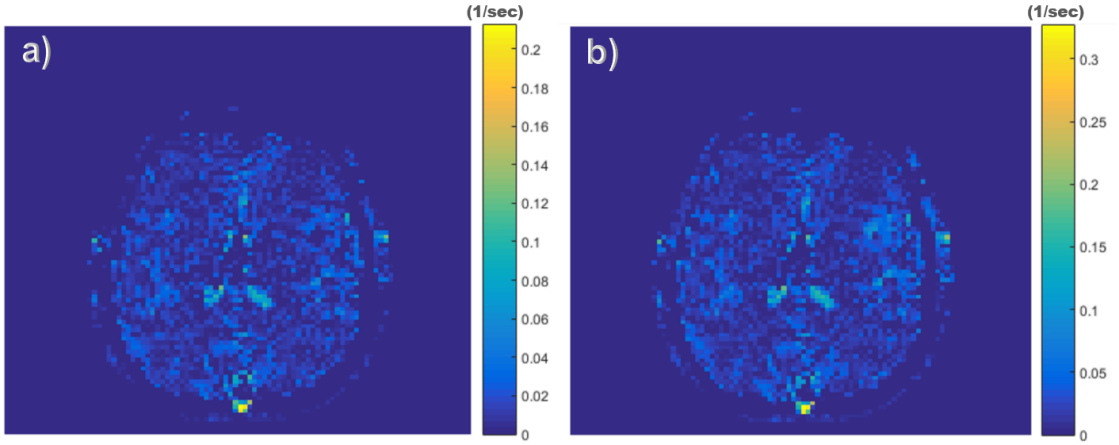

Figure 6.17: Kep resultant from model using a) uncorrected AIF b) corrected AIF for T_1 leakage effects.

Table 6.5: Kep values for tumor, gray matter and white matter while using AIF corrected and uncorrected of T_1 leakage effects.

	Tumor tissue	**Gray matter**	**White matter**
Uncorrected Kep [1/s]	0.0184	0.0205	0.0117
Corrected Kep [1/s]	0.05223	0.0409	0.0191

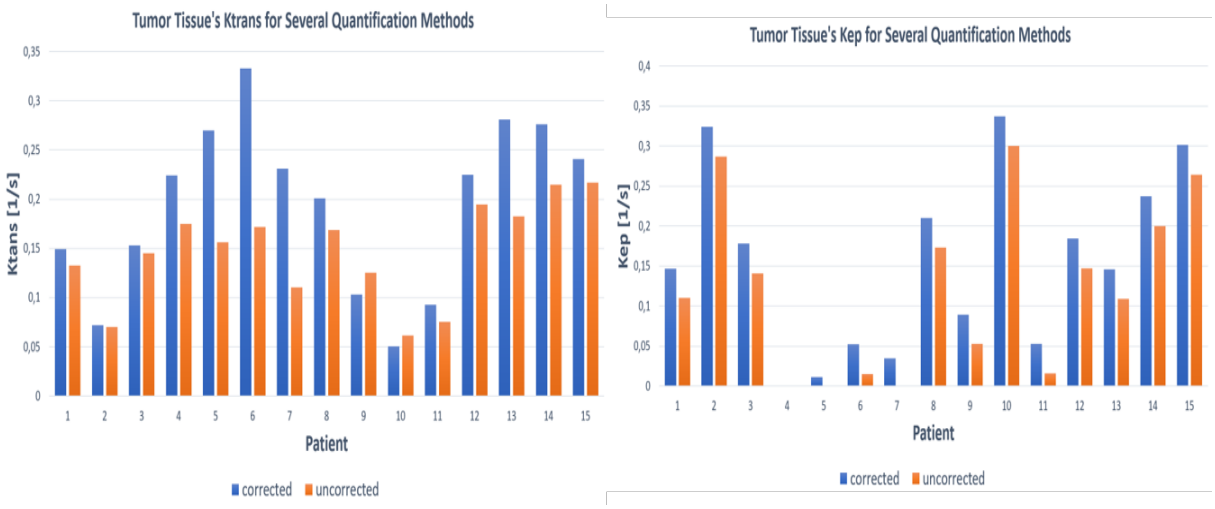

Figure 6.18: For all patients, the graphic presents K_{trans} (left) and K_{ep} (right) values for tumor tissues calculated using corrected and uncorrected data of T_1 leakage effects (left).

Next, to compare the two different methods used to calculate the ΔR_1 curves, images of each of the methods' results were provided. To clarify, image 1) results from the use of ΔR_1 where S_B was replaced with data acquired from the T_1-mapping previous to contrast injection in equation 5.19; while 2) results from the of ΔR_1 where S_B was replaced with the baseline signal of the extrapolated signal itself. A table with values of K_{trans} and K_{ep} for tumor, gray matter and white matter tissues were also included following the respective parameters maps.

As shown in Figure 6.19 and in Table 6.4, both methods outputted similar values for all three tissue types. In both methods, the tumor region is also well delimited and highlighted. This is as expected of tumor tissue since, due to angiogenesis, the BBB is disrupted in this area increasing contrast agent influx to the EES of the tumor, justifying the increase in K_{trans}.

Meanwhile, the K_{ep} parameter maps do not appear similar. On the contrary, while in method 1) the tumor area is bright, in method 2) the signal is dark and the brain structures are unclear. Despite similar values presented in Table 6.7 , it is unclear why the dissimilarities between the two images are observed in Figure 6.20. Thinking of the parameter definition, one would expect it to be the opposite of K_{trans}, therefore, the tumor region should be dark while the remaining regions ought to continue having mid range values. From a anatomical point of view, if the tissue in question does not intake any contrast then there is no contrast to leave the tissue, justifying the low values for healthy tissues. However, if the tissue allowed the passage of contrast agent into itself, these molecules will not remain inside it forever, as they ought to be excreted through the kidneys. This would make K_{ep} value as high as K_{trans}. It seems that this parameter interpretation is not set in stone and, therefore, there is no clarity of what should be expected and which conclusions to draw.

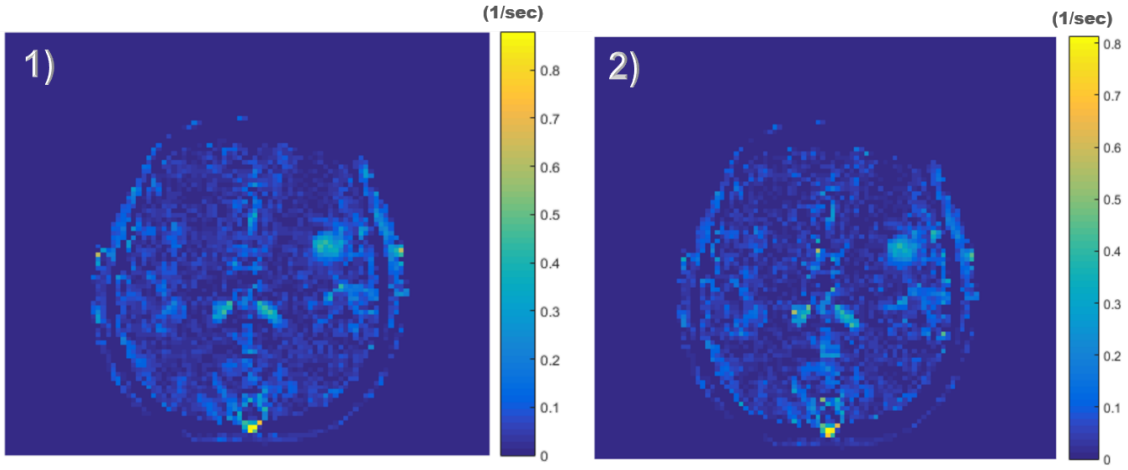

Figure 6.19: Ktrans resultant from model using 1) T1-mapping previous to contrast 2) extrapolated baseline signal.

Table 6.6: Ktrans values for tumor, gray matter and white matter for method 1) and method 2).

	Tumor tissue	**Gray matter**	**White matter**
Method 1) Ktrans [1/s]	0.3327	0.0433	0.0231
Method 2) Ktrans [1/s]	0.2962	0.0519	0.0272

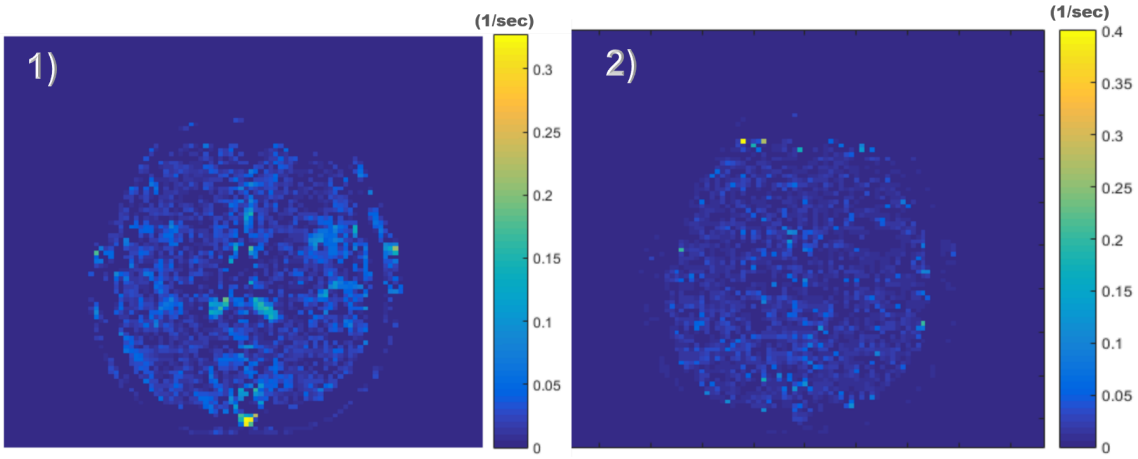

Figure 6.20: Kep resultant from model using 1) T1-mapping previous to contrast 2) extrapolated baseline signal.

Table 6.7: Kep values for tumor, gray matter and white matter for method 1) and method 2).

	Tumor tissue	**Gray matter**	**White matter**
Method 1) Kep [1/s]	0.05223	0.0409	0.0191
Method 2) Kep [1/s]	0.0708	0.0425	0.0287

For further analysis, bar graphics for each of the parameters were plotted, presenting the values for tumor, gray matter and white matter tissues of each patient. From analyzing Figure 6.21 and 6.22, it is concluded that the values from one method and the other are similar, but no more can be deduced.

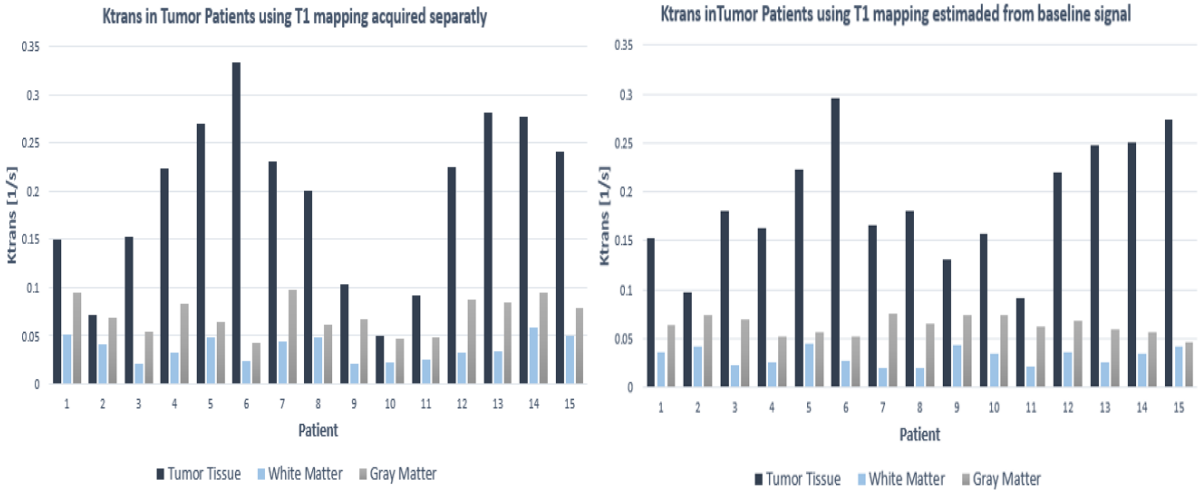

Figure 6.21: For all patients, the graphic presents K_{trans} values for three tissues: calculated using T_1-map acquired separately (left); calculated using the baseline signal from the data itself (right).

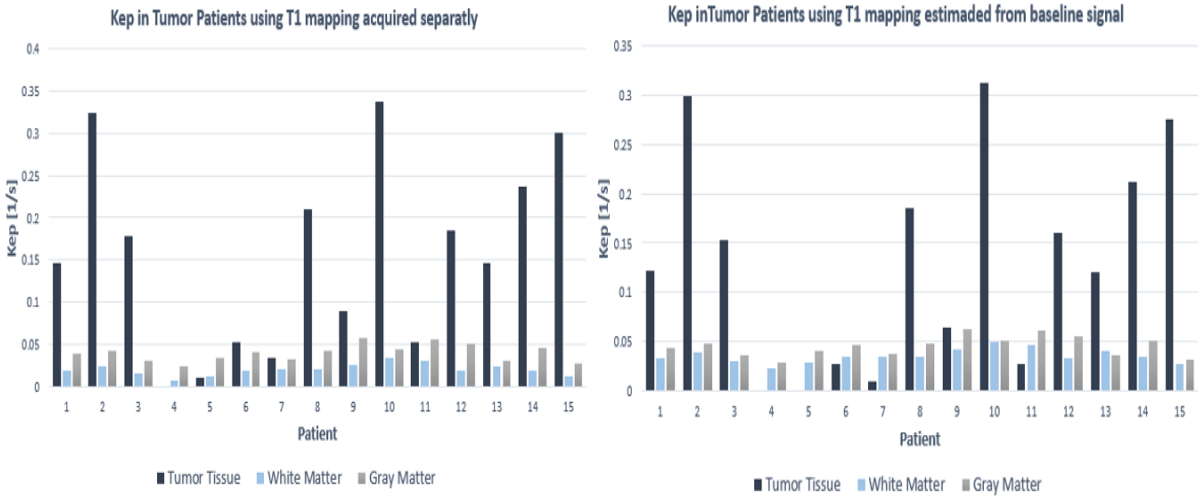

Figure 6.22: For all patients, the graphic presents K_{ep} values for three tissues: calculated using T_1-map acquired separately (left); calculated using the baseline signal from the data itself (right).

A possible source of error seems to lie in the interpretation of the models outputs. The outputs labeling seems to have generated some confusion and has led to a common misconception that the Tofts model describes tissues where the permeability for influx and outflux of contrast agent is different. This is incorrect. The permeability in all underlying models is symmetric. Several studies have reached a conclusion that, although there is some truth to the K_{trans} values, K_{ep} was introduced in the literature for notational convenience, and does not seem to have a clear physiological interpretation. In conclusion, DCE parameters have yet to become fully quantified as each study uses different sequences and applies different models, influencing the output of the results. Furthermore, each model tries to explain the inherent physiology, but makes assumptions which are not accurate and induce errors in the resulting estimated parameters.

Chapter 7

Conclusion and Future Work

Simultaneous to the ^{18}F-FET PET protocol, MRI acquisitions were performed taking advantage of the long exam time required for PET scans. This multi-modality makes the best usage of the patients time, while providing complementary information about his or hers condition. ^{18}F-FET PET images are extremely useful for confirmation of tumor presence and visual localization. While the PET images are acquired, several MRI sequence protocols can be acquired at the same time, without interference.

In this work, a T_1 recovery EPIK sequence and a SAGE-EPIK sequence simultaneous to contrast injection, were inserted in the protocol for brain tumor patients, in the Brain-PET scanner of the Forschungszentrum. Both sequences were set to output thirteen slices with a matrix size of 96×96. For each echo, 100 time points were scanned to measure time changes with a temporal resolution of 1.5 seconds.

As previously reported in [41], the estimated T_1 values from EPIK were comparable to those from other T_1-mapping sequences, correctly estimating the T_1 of white matter and gray matter tissues, reassuring its use for DCE-MRI perfusion quantification. Although several more slices could have been acquired, only thirteen were measured in order to match with the slices acquired from SAGE-EPIK.

In order to address some of the existing drawbacks and to carry a more thorough and accurate tumor investigation with perfusion parameters, the SAGE-EPI sequence method has been addressed in several studies[17], [94] and [95]. In this study, SAGE-EPIK was used, which in comparison to SAGE-EPI, provides significantly more brain coverage, better temporal resolution, shorter echo times and higher SNR for each echo, better spatial resolution and higher immunity to susceptibility artifacts. Furthermore, the multi-echo capability allows computation of T_1-corrected time series data that remove the need for a pre-bolus injection to correct for leakage effects. This is of great relevance in tumor studies, as tumor regions suffer from BBB disruption. In addition, this also allows the reduction of measurement time or the introduction of new sequences in the protocol.

The utilized SAGE-EPIK sequence consisted in the application of 5 echoes in its protocol: four gradient echos, with a refocusing pulse inbetween, and finally a spin-echo. Several studies only applied three

echoes, and stated that this is a simplified version that still provides the same information and allows leakage corrections. However, this simplified version, without the two last gradient echoes, is not less time consuming than the five echo sequence. As the SE inversion pulse is applied, before the readout pulse there is a big waiting time window required. SAGE merely takes advantage of this empty time and inserts two gradient echo pulses for further image acquisition. The main difference between these two SAGE modalities lies within the calculus method available for estimation of ΔR_2^* and ΔR_2 curve for parameters estimation.

The parametric images obtained by bolus tracking are influenced by both T_1 effects and AIF definition. To address the contrast agent extravasion, two methods were tested. Both methods successfully corrected T_1 leakage effects.
The first method was proposed by [81] and involved extrapolating the first two echoes to a TE=0, which accounts only for T_1-effects. The other method was a simplified linear fitting version from a non-linear fitting approach [82]. This method is only applicable if five echoes were acquired. This linear version reduced a lot of the processing time, but still required more time than the first method, wielding only slightly better results. Although in this work these small improvements did not justify the higher processing time, for studies which require more precision, like lower grade tumors for example, it may payout to invest in the fitting method. However, the method involving extrapolation to TE=0, also has its limitations. One drawback is its inability to correct for slice profile mismatch that can occur with spin echo sequences [17]. While this is important for absolute quantification of T_2 values, it is less important for DSC measurements that rely on assessing changes in R_2 for parameter estimation. Moreover, current SAGE-EPIK implementation quantifies slice profile mismatch during baseline, which is held constant during the dynamic time course. Thus, the effects of slice profile mismatch are effectively subtracted when ΔR_2 and ΔR_2^* are obtained for DSC purposes. Since each methods has its inherent advantages and drawbacks, accordingly to the study's objectives, the most appropriate method must be chosen. For this study, the extrapolation method was chosen. Not only was it easier and faster to implement, but accurately addressed the extravasion effects of contrast agent leakage and the overestimation of the AIF.

The AIF plays a huge role in both DSC and DCE perfusion quantification. Several methods for AIF determination have been proposed in many studies [84], [96] and [97], but their effectiveness is beyond the scope of this work. The applied approach for AIF calculation resulted from an in-house developed code which automatically searches for the best voxels that described the contrast agent delivery to the brain. In other words, automatically identifies the feeding arteries and from that, computes the AIF. This automatized process reduces the user induced errors, which would have occurred if a manual selection of the arteries was implemented for AIF determination.

For both techniques, the influence of the AIF's corrections and the performed T_1 leakage effects' corrections were investigated. Both were successfully corrected and a relevant difference in the parameters could be observed. The T_1 leakage corrections were the main source of error, inducing huge alterations in the obtained values. The tumor regions were underestimated and so were the healthy regions. This could have potentially led to the misdiagnosis of the tumor severeness, inducing a prescription of wrong treatment. Another scenario would be wrong estimation of the tumor area for surgical insight.
In the AIF estimation, the T_1 effects did not have much impact, however some influence was still detected. For the present study the impact in the pathology investigation was not substantial, however if the

tumors were smaller or of less aggressiveness, this small corrections might have been more impacting and visible.

With the correction performed, the parameters were then derived. One of the main purposes of this work was to fully quantify DSC-MRI from the implemented sequence. This objective was fulfilled, as the obtained values were in accordance with the verified literature. As expected the tumor's CBF and CBV values were higher than those of the healthy tissues, due to increase vascularization, from angiogenesis, and BBB disruption which leads to more permeability and extravasion of nutrients. The MTT parameter was not directly related to the tumor, sometimes having a higher value while other times the value was lower. Since it results from the ration of CBV and CBF, and both increase in the presence of tumor tissue, it is acceptable that the MTT values remains unchanged.

A number of sources of error can affect the parameters calculated from DSC-MRI. In this study not all were considered and it is possible that they may have affected the obtained results. A possible source of error lies in the assumption of a linear relationship between the magnetic resonance signals and the contrast's concentration. Actually, the relaxation rate measured inside arteries will vary nonlinearly and thus the linear assumption can introduce systematic errors for absolute quantification [98]. Another source of error lies in the dispersion of the bolus in patients with vascular abnormalities, as it tends to get delay or spread in time [99]. An additional source of error resides in the assumption of an uniform tissue r_2 relaxivity, where in reality tissues with different vascularization could have different relaxivities [100]. Despite the possible errors, the results seem reasonable and useful for tumor perfusion analysis.

The other main purpose of this project was to use the extrapolated data from the first two gradient echoes and achieve full DCE-MRI quantification. The data extrapolation nulls the need for two independent sequences each requiring contrast injection. Scanning time is reduced and an extra injection is, again, unnecessary. Full quantification of this technique requires a T_1- mapping previous to contrast, obtained with the EPIK inversion recovery sequence. The effectiveness and accuracy of this sequence had already been tested before in [40] and [41], and was applied with full confidence in this study. In addition, a method for DCE-MRI quantification that did not require the acquisition of the T_1-mapping, but instead extrapolated it, was also tested. Both methods outputted similar results, and the obtained values were in accordance with the available literature. The applied kinetic model for DCE-quantification, the Tofts model, was chosen for its simplicity and wide use in brain perfusion studies. However only one of the obtained parameters showed correctness, the K_{trans} parameter. Meanwhile the K_{ep} parameter results were unclear in its meaning and showed some discrepancies. It was searched in the literature, and it seems that this parameter was introduced in the literature for nomenclature's convenience, hence it does not have a clear physiological interpretation [71].

The biggest error source in DCE-MRI is, as observed, the kinetic model. On one hand, simplistic models introduce systematic errors into the kinetic parameters by overlooking some perfusion physiology parameters. On the other hand, complex models, include too many variables which cause difficulties in data acquisition and analyses, making the models almost impossible to apply.

Another source of errors lies, as similarly to DSC-MRI, in the assumption that relaxivity of the contrast agent is constant for every tissue, when in reality it differs. An additional factor which greatly influences DCE derived data is the trade-off between temporal and spacial resolution, both required for precise

model application. In conclusion, there is a lot of room for improvement in full DCE-MRI quantification, where model accuracy and precision must be fully investigated to prove its assertiveness with reality.

Nowadays, several studies have tried correlating the perfusion techniques derived parameters, with the tumor grade or its response with therapy in order to avoid the need for invasive biopsies. Although not an objective of this study, if possible it would have been a great addition to the developed work to further investigate this possible correlation. However, this would require knowledge of the actual tumor grade or histology which was not available for all patients, and therefore, not further investigated.

Summing up, the main objectives of this study were successfully reached, despite the referred shortcomings. The major source of error of this work lies in the applied kinetic models, both for DSC- and DCE-MRI. To mitigate this source of error, a more intense and thorough investigation on this matter must be performed. Not just testing the models, but actually finding a way to measure the real perfusion values in order to establish the ground truth parameter's values. The development of a perfusion phantom would be the main solution for this scenario.

References

[1] Burton P Drayer, E Ralph Heinz, Manual Dujovny, Jr SK Wolfson, and David Gur. Patterns of brain perfusion: dynamic computed tomography using intravenous contrast enhancement. *Journal of computer assisted tomography*, 3(5):633–640, 1979.

[2] David Norman, Leon Axel, Walter H Berninger, Michael S Edwards, Christopher E Cann, Rowland W Redington, and Lauranne Cox. Dynamic computed tomography of the brain: techniques, data analysis, and applications. *American Journal of Roentgenology*, 136(4):759–770, 1981.

[3] WD Heiss, K Herholz, HG Böcher-Schwarz, G Pawlik, K Wienhard, W Steinbrich, and G Friedmann. Pet, ct, and mr imaging in cerebrovascular disease. *Journal of computer assisted tomography*, 10(6):903–911, 1986.

[4] Harry T Chugani, Michael E Phelps, and John C Mazziotta. Positron emission tomography study of human brain functional development. *Brain development and cognition: A reader*, pages 101–116, 2002.

[5] Wolfram H Knapp, Rüdiger von Kummer, and Wolfgang Kübler. Imaging of cerebral blood flow-to-volume distribution using spect. *Journal of nuclear medicine*, 27(4):465–470, 1986.

[6] Geraint Rees, A Howseman, Oliver Josephs, Chris D Frith, Karl J Friston, Richard SJ Frackowiak, and Robert Turner. Characterizing the relationship between bold contrast and regional cerebral blood flow measurements by varying the stimulus presentation rate. *Neuroimage*, 6(4):270–278, 1997.

[7] Moran Artzi, Deborah T Blumenthal, Felix Bokstein, Guy Nadav, Gilad Liberman, Orna Aizenstein, and Dafna Ben Bashat. Classification of tumor area using combined dce and dsc mri in patients with glioblastoma. *Journal of neuro-oncology*, 121(2):349–357, 2015.

[8] M Bergamino, L Bonzano, F Levrero, GL Mancardi, and L Roccatagliata. A review of technical aspects of t1-weighted dynamic contrast-enhanced magnetic resonance imaging (dce-mri) in human brain tumors. *Physica Medica*, 30(6):635–643, 2014.

[9] Eric S Paulson and Kathleen M Schmainda. Comparison of dynamic susceptibility-weighted contrast-enhanced mr methods: recommendations for measuring relative cerebral blood volume in brain tumors. *Radiology*, 249(2):601–613, 2008.

[10] Valerij G Kiselev. On the theoretical basis of perfusion measurements by dynamic susceptibility contrast mri. *Magnetic Resonance in Medicine: An Official Journal of the International Society for Magnetic Resonance in Medicine*, 46(6):1113–1122, 2001.

[11] Panagiotis Tsialios, Michael Thrippleton, A Glatz, and C Pernet. Evaluation of mri sequences for quantitative t1 brain mapping. In *Journal of Physics: Conference Series*, volume 931, page 012038. IOP Publishing, 2017.

[12] Thomas E Yankeelov and John C Gore. Dynamic contrast enhanced magnetic resonance imaging in oncology: theory, data acquisition, analysis, and examples. *Current medical imaging reviews*, 3(2):91–107, 2007.

[13] CC Quarles, BD Ward, and KM Schmainda. Improving the reliability of obtaining tumor hemodynamic parameters in the presence of contrast agent extravasation. *Magnetic Resonance in Medicine: An Official Journal of the International Society for Magnetic Resonance in Medicine*, 53(6):1307–1316, 2005.

[14] RM Weisskoff, JL Boxerman, AG Sorensen, SM Kulke, TA Campbell, and BR Rosen. Simultaneous blood volume and permeability mapping using a single gd-based contrast injection. In *Proceedings of the Society of Magnetic Resonance, Second Annual Meeting*, pages 6–12, 1994.

[15] A Gregory Sorensen and Peter Reimer. Cerebral mr perfusion imaging: principles and current applications. 2000.

[16] Rexford D Newbould, Stefan T Skare, Thies H Jochimsen, Marcus T Alley, Michael E Moseley, Gregory W Albers, and Roland Bammer. Perfusion mapping with multiecho multishot parallel imaging epi. *Magnetic Resonance in Medicine: An Official Journal of the International Society for Magnetic Resonance in Medicine*, 58(1):70–81, 2007.

[17] Heiko Schmiedeskamp, Matus Straka, Rexford D Newbould, Greg Zaharchuk, Jalal B Andre, Jean-Marc Olivot, Michael E Moseley, Gregory W Albers, and Roland Bammer. Combined spin- and gradient-echo perfusion-weighted imaging. *Magnetic resonance in medicine*, 68(1):30–40, 2012.

[18] Nuno Silva. Methods for molecular imaging with mr-pet. 2017.

[19] Robert J Gillies, Zaver M Bhujwalla, Jeffrey Evelhoch, Michael Garwood, Michal Neema, Simon P Robinson, Christopher H Sotak, and Boudewijn Van Der Sanden. Applications of magnetic resonance in model systems: tumor biology and physiology. *Neoplasia*, 2(1-2):139–151, 2000.

[20] Jeffrey L Evelhoch, Robert J Gillies, Gregory S Karczmar, Jason A Koutcher, Ross J Maxwell, Orhan Nalcioglu, Natarajan Raghunand, Sabrina M Ronen, Brian D Ross, and Harold M Swartz. Applications of magnetic resonance in model systems: cancer therapeutics. *Neoplasia*, 2(1-2): 152–165, 2000.

[21] Peter Caravan, Jeffrey J Ellison, Thomas J McMurry, and Randall B Lauffer. Gadolinium (iii) chelates as mri contrast agents: structure, dynamics, and applications. *Chemical reviews*, 99(9): 2293–2352, 1999.

[22] Brian M Dale, Mark A Brown, and Richard C Semelka. *MRI: basic principles and applications*. John Wiley & Sons, 2015.

[23] Felix Bloch. Nuclear induction. *Physical review*, 70(7-8):460, 1946.

[24] Dwight George Nishimura. *Principles of magnetic resonance imaging*. Stanford University, 1996.

[25] Govind B Chavhan, Paul S Babyn, Bejoy Thomas, Manohar M Shroff, and E Mark Haacke. Principles, techniques, and applications of t2*-based mr imaging and its special applications. *Radiographics*, 29(5):1433–1449, 2009.

[26] Yi. Mri concept. URL `https://nmrimaging.wordpress.com/tag/medical-imaging/`.

[27] Paul C Lauterbur et al. Image formation by induced local interactions: examples employing nuclear magnetic resonance. 1973.

[28] Anil Kumar, Dieter Welti, and Richard R Ernst. Nmr fourier zeugmatography. *Journal of Magnetic Resonance (1969)*, 18(1):69–83, 1975.

[29] Peter Mansfield. Multi-planar image formation using nmr spin echoes. *Journal of Physics C: Solid State Physics*, 10(3):L55, 1977.

[30] A Lascialfari, F Filibian, C Sangregorio, and P Carretta. In vivo biomedical applications of magnetic resonance and magnetic materials. *Riv. Nuovo Cimento*, 36:211–271, 2013.

[31] Stig Ljunggren. Imaging methods. *Journal of Magnetic Resonance*, 54:338–343, 1983.

[32] Donald B Twieg. The k-trajectory formulation of the nmr imaging process with applications in analysis and synthesis of imaging methods. *Medical physics*, 10(5):610–621, 1983.

[33] Reuben Mezrich. A perspective on k-space. *Radiology*, 195(2):297–315, 1995.

[34] Chunlei Liu, Michael E Moseley, and Roland Bammer. Simultaneous phase correction and sense reconstruction for navigated multi-shot dwi with non-cartesian k-space sampling. *Magnetic resonance in medicine*, 54(6):1412–1422, 2005.

[35] Maleah Tenison. Principles of nuclear magnetic resonance and mri review - ppt download. URL `https://slideplayer.com/slide/3279728/`.

[36] Jascha D Swisher, John A Sexton, J Christopher Gatenby, John C Gore, and Frank Tong. Multishot versus single-shot pulse sequences in very high field fmri: a comparison using retinotopic mapping. *PloS one*, 7(4):e34626, 2012.

[37] Maxim Zaitsev, K Zilles, and NJ Shah. Shared k-space echo planar imaging with keyhole. *Magnetic Resonance in Medicine: An Official Journal of the International Society for Magnetic Resonance in Medicine*, 45(1):109–117, 2001.

[38] Robert L Barry, L Martyn Klassen, Joy M Williams, and Ravi S Menon. Hybrid two-dimensional navigator correction: a new technique to suppress respiratory-induced physiological noise in multi-shot echo-planar functional mri. *Neuroimage*, 39(3):1142–1150, 2008.

[39] Joop J Van Vaals, Marijn E Brummer, W Thomas Dixon, Hans H Tuithof, Hans Engels, Rendon C Nelson, Brigid M Gerety, Judith L Chezmar, and Jacques A Den Boer. "keyhole" method for accelerating imaging of contrast agent uptake. *Journal of Magnetic Resonance Imaging*, 3(4): 671–675, 1993.

[40] Seong Dae Yun, Martina Reske, Kaveh Vahedipour, Tracy Warbrick, and N Jon Shah. Parallel imaging acceleration of epik for reduced image distortions in fmri. *Neuroimage*, 73:135–143, 2013.

[41] Seong Dae Yun and N Jon Shah. Whole-brain high in-plane resolution fmri using accelerated epik for enhanced characterisation of functional areas at 3t. *PloS one*, 12(9):e0184759, 2017.

[42] RJ Ordidge, P Gibbs, B Chapman, MK Stehling, and P Mansfield. High-speed multislice t1 mapping using inversion-recovery echo-planar imaging. *Magnetic resonance in medicine*, 16(2): 238–245, 1990.

[43] AJ Freeman, PA Gowland, and P Mansfield. Optimization of the ultrafast look-locker echo-planar imaging t1 mapping sequence. *Magnetic resonance imaging*, 16(7):765–772, 1998.

[44] Jon M. Shah and Yun Seong Dae. A rapid whole-brain look-locker method for t1 mapping using inversion recovery epik. *Proc. Intl. Soc. Mag. Reson. Med*, 25, 2017.

[45] Kathleen M Donahue, Hendrikus GJ Krouwer, Scott D Rand, Arvind P Pathak, Cathy S Marszalkowski, Steven C Censky, and Robert W Prost. Utility of simultaneously acquired gradient-echo and spin-echo cerebral blood volume and morphology maps in brain tumor patients. *Magnetic resonance in medicine*, 43(6):845–853, 2000.

[46] Kathleen M Schmainda, Scott D Rand, Allen M Joseph, Rebecca Lund, B Doug Ward, Arvind P Pathak, John L Ulmer, Michael A Baddrudoja, and Hendrikus GJ Krouwer. Characterization of a first-pass gradient-echo spin-echo method to predict brain tumor grade and angiogenesis. *American Journal of Neuroradiology*, 25(9):1524–1532, 2004.

[47] Bruce E Hammer, Nelson L Christensen, and Brian G Heil. Use of a magnetic field to increase the spatial resolution of positron emission tomography. *Medical physics*, 21(12):1917–1920, 1994.

[48] Yiping Shao, Simon R Cherry, Keyvan Farahani, Ken Meadors, Stefan Siegel, Robert W Silverman, and Paul K Marsden. Simultaneous pet and mr imaging. *Physics in Medicine & Biology*, 42 (10):1965, 1997.

[49] Heinz-Peter W Schlemmer, Bernd J Pichler, Matthias Schmand, Ziad Burbar, Christian Michel, Ralf Ladebeck, Kirstin Jattke, David Townsend, Claude Nahmias, Pradeep K Jacob, et al. Simultaneous mr/pet imaging of the human brain: feasibility study. *Radiology*, 248(3):1028–1035, 2008.

[50] Frederich H Martini, Judi L Nath, and Edwin F Bartholomew. *Anatomy and physiology*. New York: Prentice Hall, 2005.

[51] Domenico Ribatti, Angelo Vacca, and Marco Presta. The discovery of angiogenic factors:: A historical review. *General Pharmacology: The Vascular System*, 35(5):227–231, 2000.

[52] Judah Folkman. Angiogenesis in cancer, vascular, rheumatoid and other disease. *Nature medicine*, 1(1):27, 1995.

[53] Ngoc H On, Ryan Mitchell, Sanjot D Savant, Corbin J Bachmeier, Grant M Hatch, and Donald W Miller. Examination of blood–brain barrier (bbb) integrity in a mouse brain tumor model. *Journal of neuro-oncology*, 111(2):133–143, 2013.

[54] Anna K Heye, Ross D Culling, Maria del C Valdés Hernández, Michael J Thrippleton, and Joanna M Wardlaw. Assessment of blood–brain barrier disruption using dynamic contrast-enhanced mri. a systematic review. *NeuroImage: Clinical*, 6:262–274, 2014.

[55] David N Louis, Arie Perry, Guido Reifenberger, Andreas Von Deimling, Dominique Figarella-Branger, Webster K Cavenee, Hiroko Ohgaki, Otmar D Wiestler, Paul Kleihues, and David W Ellison. The 2016 world health organization classification of tumors of the central nervous system: a summary. *Acta neuropathologica*, 131(6):803–820, 2016.

[56] Garry Ceccon, Philipp Lohmann, Gabriele Stoffels, Natalie Judov, Christian P Filss, Marion Rapp, Elena Bauer, Christina Hamisch, Maximilian I Ruge, Martin Kocher, et al. Dynamic o-(2-18f-fluoroethyl)-l-tyrosine positron emission tomography differentiates brain metastasis recurrence from radiation injury after radiotherapy. *Neuro-oncology*, 19(2):281–288, 2016.

[57] Norbert Galldiks, Veronika Dunkl, Gabriele Stoffels, Markus Hutterer, Marion Rapp, Michael Sabel, Guido Reifenberger, Sied Kebir, Franziska Dorn, Tobias Blau, et al. Diagnosis of pseudoprogression in patients with glioblastoma using o-(2-[18 f] fluoroethyl)-l-tyrosine pet. *European journal of nuclear medicine and molecular imaging*, 42(5):685–695, 2015.

[58] Philipp Lohmann, Gabriele Stoffels, Garry Ceccon, Marion Rapp, Michael Sabel, Christian P Filss, Marcel A Kamp, Carina Stegmayr, Bernd Neumaier, Nadim J Shah, et al. Radiation injury vs. recurrent brain metastasis: combining textural feature radiomics analysis and standard parameters may increase 18f-fet pet accuracy without dynamic scans. *European radiology*, 27(7): 2916–2927, 2017.

[59] Ingrid S Gribbestad, Kjell I Gjesdal, Gunnar Nilsen, Steinar Lundgren, Mari HB Hjelstuen, and Alan Jackson. An introduction to dynamic contrast-enhanced mri in oncology. In *Dynamic contrast-enhanced magnetic resonance imaging in oncology*, pages 1–22. Springer, 2005.

[60] Thomas Fritz-Hansen, Egill Rostrup, Henrik BW Larsson, Lars Søndergaard, Poul Ring, and Ole Henriksen. Measurement of the arterial concentration of gd-dtpa using mri: a step toward quantitative perfusion imaging. *Magnetic Resonance in Medicine*, 36(2):225–231, 1996.

[61] Nicholas E Simpson, Zhanquan He, and Jeffrey L Evelhoch. Deuterium nmr tissue perfusion measurements using the tracer uptake approach: I. optimization of methods. *Magnetic Resonance in Medicine: An Official Journal of the International Society for Magnetic Resonance in Medicine*, 42(1):42–52, 1999.

[62] SS Kety. Peripheral blood flow measurement. *Pharmacol Rev*, 3(1):1–41, 1951.

[63] Chen Lin. R perfusion imaging techniques and applications, 2009. URL `http://www.indiana.edu/~mri/CE/slides/MRPerfusionTechniquesandApplications090714.pdf`.

[64] Paul Meier and Kenneth L Zierler. On the theory of the indicator-dilution method for measurement of blood flow and volume. *Journal of applied physiology*, 6(12):731–744, 1954.

[65] Leif Østergaard, Robert M Weisskoff, David A Chesler, Carsten Gyldensted, and Bruce R Rosen. High resolution measurement of cerebral blood flow using intravascular tracer bolus passages. part i: Mathematical approach and statistical analysis. *Magnetic resonance in medicine*, 36(5): 715–725, 1996.

[66] Lisa Willats and Fernando Calamante. The 39 steps: evading error and deciphering the secrets for accurate dynamic susceptibility contrast mri. *NMR in Biomedicine*, 26(8):913–931, 2013.

[67] Paul S Tofts, Gunnar Brix, David L Buckley, Jeffrey L Evelhoch, Elizabeth Henderson, Michael V Knopp, Henrik BW Larsson, Ting-Yim Lee, Nina A Mayr, Geoffrey JM Parker, et al. Estimating kinetic parameters from dynamic contrast-enhanced t1-weighted mri of a diffusable tracer: standardized quantities and symbols. *Journal of Magnetic Resonance Imaging: An Official Journal of the International Society for Magnetic Resonance in Medicine*, 10(3):223–232, 1999.

[68] Rebecca AP Dijkhoff, Monique Maas, Milou H Martens, Nikolaos Papanikolaou, Doenja MJ Lambregts, Geerard L Beets, and Regina GH Beets-Tan. Correlation between quantitative and semiquantitative parameters in dce-mri with a blood pool agent in rectal cancer: can semiquantitative parameters be used as a surrogate for quantitative parameters? *Abdominal Radiology*, 42 (5):1342–1349, 2017.

[69] Fahmi Khalifa, Ahmed Soliman, Ayman El-Baz, Mohamed Abou El-Ghar, Tarek El-Diasty, Georgy Gimel'farb, Rosemary Ouseph, and Amy C Dwyer. Models and methods for analyzing dce-mri: A review. *Medical physics*, 41(12), 2014.

[70] June S Taylor, Paul S Tofts, Ruediger Port, Jeffrey L Evelhoch, Michael Knopp, Wilburn E Reddick, Val M Runge, and Nina Mayr. Mr imaging of tumor microcirculation: promise for the new millenium. *Journal of Magnetic Resonance Imaging: An Official Journal of the International Society for Magnetic Resonance in Medicine*, 10(6):903–907, 1999.

[71] Steven P Sourbron and David L Buckley. Classic models for dynamic contrast-enhanced mri. *NMR in Biomedicine*, 26(8):1004–1027, 2013.

[72] Christian P Filss, Norbert Galldiks, Gabriele Stoffels, Michael Sabel, Hans J Wittsack, Bernd Turowski, Gerald Antoch, Ke Zhang, Gereon R Fink, Heinz H Coenen, et al. Comparison of 18f-fet pet and perfusion-weighted mr imaging: a pet/mr imaging hybrid study in patients with brain tumors. *J Nucl Med*, 55(4):540–545, 2014.

[73] Floris HP van Velden, Reina W Kloet, Bart NM van Berckel, Saskia PA Wolfensberger, Adriaan A Lammertsma, and Ronald Boellaard. Comparison of 3d-op-osem and 3d-fbp reconstruction algorithms for high-resolution research tomograph studies: effects of randoms estimation methods. *Physics in Medicine & Biology*, 53(12):3217, 2008.

[74] Robert L Braun and Alan K Burnham. Pmod: a flexible model of oil and gas generation, cracking, and expulsion. *Organic Geochemistry*, 19(1-3):161–172, 1992.

[75] H Herzog, K-J Langen, C Weirich, E Rota Kops, J Kaffanke, L Tellmann, J Scheins, I Neuner, G Stoffels, K Fischer, et al. High resolution brainpet combined with simultaneous mri. *Nuklearmedizin*, 50(02):74–82, 2011.

[76] MATLAB User's Guide. The mathworks. *Inc., Natick, MA*, 5:333, 1998.

[77] Julio Cárdenas-Rodríguez, Christine M Howison, and Mark D Pagel. A linear algorithm of the reference region model for dce-mri is robust and relaxes requirements for temporal resolution. *Magnetic resonance imaging*, 31(4):497–507, 2013.

[78] Andreas Markus Loening and Sanjiv Sam Gambhir. Amide: a free software tool for multimodality medical image analysis. *Molecular imaging*, 2(3):15353500200303133, 2003.

[79] Bruce R Rosen, John W Belliveau, James M Vevea, and Thomas J Brady. Perfusion imaging with nmr contrast agents. *Magnetic resonance in medicine*, 14(2):249–265, 1990.

[80] E Kanal, K Maravilla, and HA Rowley. Gadolinium contrast agents for cns imaging: current concepts and clinical evidence. *American Journal of Neuroradiology*, 2014.

[81] Evert-jan Ph A Vonken, Matthias JP van Osch, Chris JG Bakker, and Max A Viergever. Simultaneous quantitative cerebral perfusion and gd-dtpa extravasation measurement with dual-echo dynamic susceptibility contrast mri. *Magnetic resonance in Medicine*, 43(6):820–827, 2000.

[82] Heiko Schmiedeskamp, Matus Straka, and Roland Bammer. Compensation of slice profile mismatch in combined spin-and gradient-echo echo-planar imaging pulse sequences. *Magnetic resonance in medicine*, 67(2):378–388, 2012.

[83] Nobuyuki Otsu. A threshold selection method from gray-level histograms. *IEEE transactions on systems, man, and cybernetics*, 9(1):62–66, 1979.

[84] Fernando Calamante. Arterial input function in perfusion mri: a comprehensive review. *Progress in nuclear magnetic resonance spectroscopy*, 74:1–32, 2013.

[85] Marko K Ivancevic, Ivan Zimine, Xavier Montet, Jean-Noel Hyacinthe, François Lazeyras, David Foxall, and Jean-Paul Vallée. Inflow effect correction in fast gradient-echo perfusion imaging. *Magnetic Resonance in Medicine: An Official Journal of the International Society for Magnetic Resonance in Medicine*, 50(5):885–891, 2003.

[86] Louisa Bokacheva, Henry Rusinek, Qun Chen, Niels Oesingmann, Chekema Prince, Manmeen Kaur, Elissa Kramer, and Vivian S Lee. Quantitative determination of gd-dtpa concentration in

t1-weighted mr renography studies. *Magnetic Resonance in Medicine: An Official Journal of the International Society for Magnetic Resonance in Medicine*, 57(6):1012–1018, 2007.

[87] Melanie Heilmann, Fabian Kiessling, Marta Enderlin, and Lothar R Schad. Determination of pharmacokinetic parameters in dce mri: consequence of nonlinearity between contrast agent concentration and signal intensity. *Investigative radiology*, 41(6):536–543, 2006.

[88] Jean-François Adam, Hélène Elleaume, Géraldine Le Duc, Stéphanie Corde, Anne-Marie Charvet, Irène Troprès, Jean-François Le Bas, and François Estève. Absolute cerebral blood volume and blood flow measurements based on synchrotron radiation quantitative computed tomography. *Journal of Cerebral Blood Flow & Metabolism*, 23(4):499–512, 2003.

[89] Anne M Smith, Cécile B Grandin, Thierry Duprez, Frédéric Mataigne, and Guy Cosnard. Whole brain quantitative cbf and cbv measurements using mri bolus tracking: comparison of methodologies. *Magnetic Resonance in Medicine: An Official Journal of the International Society for Magnetic Resonance in Medicine*, 43(4):559–564, 2000.

[90] B Wang, B Zhao, Y Zhang, M Ge, P Zhao, C Li, Q Pang, S Xu, Y Liu, et al. Absolute cbv for the differentiation of recurrence and radionecrosis of brain metastases after gamma knife radiotherapy: a comparison with relative cbv. *Clinical radiology*, 2018.

[91] Evelynn Vergauwen, Anne-Marie Vanbinst, Carola Brussaard, Peter Janssens, Dieter De Clerck, Michel Van Lint, Anne C Houtman, Olaf Michel, Kathelijn Keymolen, Bieke Lefevere, et al. Central nervous system gadolinium accumulation in patients undergoing periodical contrast mri screening for hereditary tumor syndromes. *Hereditary cancer in clinical practice*, 16(1):2, 2018.

[92] Marios Spanakis, Eleftherios Kontopodis, Sophie Van Cauter, Vangelis Sakkalis, and Kostas Marias. Assessment of dce–mri parameters for brain tumors through implementation of physiologically–based pharmacokinetic model approaches for gd-dota. *Journal of pharmacokinetics and pharmacodynamics*, 43(5):529–547, 2016.

[93] Tufail F Patankar, Hamied A Haroon, Samantha J Mills, Danielle Balériaux, David L Buckley, Geoff JM Parker, and Alan Jackson. Is volume transfer coefficient (ktrans) related to histologic grade in human gliomas? *American Journal of Neuroradiology*, 26(10):2455–2465, 2005.

[94] Heiko Schmiedeskamp, Jalal B Andre, Matus Straka, Thomas Christen, Seema Nagpal, Lawrence Recht, Reena P Thomas, Greg Zaharchuk, and Roland Bammer. Simultaneous perfusion and permeability measurements using combined spin-and gradient-echo mri. *Journal of Cerebral Blood Flow & Metabolism*, 33(5):732–743, 2013.

[95] Ashley M Stokes, Jack T Skinner, and C Chad Quarles. Assessment of a combined spin-and gradient-echo (sage) dsc-mri method for preclinical neuroimaging. *Magnetic resonance imaging*, 32(10):1181–1190, 2014.

[96] Jeremy Chen, Jianhua Yao, and David Thomasson. Automatic determination of arterial input function for dynamic contrast enhanced mri in tumor assessment. In *International Conference on Medical Image Computing and Computer-Assisted Intervention*, pages 594–601. Springer, 2008.

[97] Lisa Willats, Soren Christensen, Henry K Ma, Geoffrey A Donnan, Alan Connelly, and Fernando Calamante. Validating a local arterial input function method for improved perfusion quantification in stroke. *Journal of Cerebral Blood Flow & Metabolism*, 31(11):2189–2198, 2011.

[98] Fernando Calamante, Alan Connelly, and Matthias JP van Osch. Nonlinear δr effects in perfusion quantification using bolus-tracking mri. *Magnetic Resonance in Medicine: An Official Journal of the International Society for Magnetic Resonance in Medicine*, 61(2):486–492, 2009.

[99] Fernando Calamante, Lisa Willats, David G Gadian, and Alan Connelly. Bolus delay and dispersion in perfusion mri: implications for tissue predictor models in stroke. *Magnetic Resonance in Medicine: An Official Journal of the International Society for Magnetic Resonance in Medicine*, 55(5):1180–1185, 2006.

[100] Jerrold L Boxerman, Leena M Hamberg, Bruce R Rosen, and Robert M Weisskoff. Mr contrast due to intravascular magnetic susceptibility perturbations. *Magnetic Resonance in Medicine*, 34 (4):555–566, 1995.

Appendix

Patient	Gender	Histology &Tumor grading
1	Female	Glioblastoma – IV
2	Male	Oligodendroglioma – II
3	Female	Anaplastic Astrocytoma -III
4	Male	Unknown
5	Female	Glioblastoma – IV
6	Male	Glioblastoma - IV
7	Male	Unknown
8	Female	Unknown
9	Female	Unknown
10	Male	Unknown
11	Female	Unknown
12	Male	Unknown
13	Female	Unknown
14	Male	Unknown
15	Male	Unknown

Figure 7.1: Available information relative to the patients used in this study.